Monthly Notices
of the
ROYAL ASTRONOMICAL SOCIETY

MNRAS **498,** 2167–2195 (2020)
Advance Access publication 2020 August 19

doi:10.1093/mnras/staa2351

AT 2017gbl: a dust obscured TDE candidate in a luminous infrared galaxy

E. C. Kool [1,2★] T. M. Reynolds [3] S. Mattila,[3] E. Kankare,[3] M. A. Pérez-Torres,[4] A. Efstathiou,[5] S. Ryder [2] C. Romero-Cañizales,[6,7] W. Lu [8] T. Heikkilä,[3] G. E. Anderson [9] M. Berton [10,11] J. Bright [12] G. Cannizzaro [13,14] D. Eappachen,[13,14] M. Fraser [15] M. Gromadzki,[16] P. G. Jonker,[13,14] H. Kuncarayakti,[3,10] P. Lundqvist [1] K. Maeda,[17] R. M. McDermid,[2] A. M. Medling [18,19] S. Moran,[3] A. Reguitti [20,21,22] M. Shahbandeh,[23] S. Tsygankov,[3,24] V. U[25] and T. Wevers [26]

Affiliations are listed at the end of the paper

Accepted 2020 August 3. Received 2020 August 3; in original form 2020 March 5

ABSTRACT

We present the discovery with Keck of the extremely infrared (IR) luminous transient AT 2017gbl, coincident with the Northern nucleus of the luminous infrared galaxy (LIRG) IRAS 23436+5257. Our extensive multiwavelength follow-up spans ∼900 d, including photometry and spectroscopy in the optical and IR, and (very long baseline interferometry) radio and X-ray observations. Radiative transfer modelling of the host galaxy spectral energy distribution and long-term pre-outburst variability in the mid-IR indicate the presence of a hitherto undetected dust obscured active galactic nucleus (AGN). The optical and near-IR spectra show broad ∼2000 km s^{-1} hydrogen, He I, and O I emission features that decrease in flux over time. Radio imaging shows a fast evolving compact source of synchrotron emission spatially coincident with AT 2017gbl. We infer a lower limit for the radiated energy of 7.3×10^{50} erg from the IR photometry. An extremely energetic supernova would satisfy this budget, but is ruled out by the radio counterpart evolution. Instead, we propose AT 2017gbl is related to an accretion event by the central supermassive black hole, where the spectral signatures originate in the AGN broad line region and the IR photometry is consistent with re-radiation by polar dust. Given the fast evolution of AT 2017gbl, we deem a tidal disruption event (TDE) of a star a more plausible scenario than a dramatic change in the AGN accretion rate. This makes AT 2017gbl the third TDE candidate to be hosted by a LIRG, in contrast to the so far considered TDE population discovered at optical wavelengths and hosted preferably by post-starburst galaxies.

Key words: accretion, accretion discs – black hole physics – galaxies: active – galaxies: nuclei – transients: tidal disruption events.

1 INTRODUCTION

Nuclear variability in galaxies is often attributed to the presence of an active galactic nucleus (AGN), where matter is accreted by a central supermassive black hole (SMBH). AGNs are known to be intrinsically variable, where the amplitude and time-scale depend on the wavelength of observation. AGN typically show small-amplitude stochastic variability in brightness of <40 per cent in the optical (Kelly, Bechtold & Siemiginowska 2009), whereas in the mid-infrared (IR) AGN show larger and smoother variability on longer time-scales of years to decades (Kozłowski et al. 2016). However, an increasing number of nuclear outbursts are being observed that do not fit in this picture, showing large amplitude variability on a short time-scale, both by galaxies with an AGN and by inactive galaxies. The interpretations of these events have included a tidal disruption event (TDE) of a star by a SMBH, or major changes in the accretion rate of an SMBH that result in changes in AGN spectra (changing look AGN, or CLAGN). Supernovae (SNe) have also been suggested, since (core-collapse) SNe are expected in the nuclear regions of starburst and luminous infrared galaxies (LIRGs; $L_{\rm IR} > 10^{11}$ L$_\odot$) at rates a couple of orders of magnitude higher than in normal field galaxies (Pérez-Torres et al. 2009b; Kankare et al. 2012; Mattila et al. 2012; Kool et al. 2018).

TDEs were theoretically predicted over forty years ago (Hills 1975; Rees 1988), and are expected to give rise to a luminous flare typically peaking in the X-ray/UV/optical. Over the past ten years a number of optical TDE candidates have been discovered, often with concurrent detections at X-ray, UV, or radio wavelengths (Bade, Komossa & Dahlem 1996; Zauderer et al. 2011; Gezari et al. 2012; van Velzen et al. 2020). van Velzen (2018) found a roughly constant volumetric rate for these events for BHs with masses below $10^{7.5}$ M$_\odot$, followed by a sharp drop for more massive black holes, which directly capture stars without a luminous flare. One notable feature of the population of optically discovered TDEs is that they seem to show a preference for E+A galaxies (Arcavi et al. 2014; French, Arcavi & Zabludoff 2016), a class of post-starburst galaxies that are thought to be the result of a merger that occurred approximately 10^9 yr previously (Dressler & Gunn 1983). It has been suggested, based on simulations, that this overabundance is a result of the presence of a secondary (in-spiralling) SMBH enhancing the TDE rate by several orders of magnitude for a period of 10^4–10^5 yr (Chen et al. 2009; Cen 2020) and as such is intrinsic to post-merger galaxies. However,

★ E-mail: erik.kool@astro.su.se

based on a study of four TDE host galaxies, French et al. (2020) suggested high central stellar densities are a more important driver for increased TDE rates.

Most discovered TDEs seem to suffer from negligible host galaxy extinction, which could suggest a selection bias in the predominantly optical/UV discovered TDE sample. The discovery of (candidate) TDEs in LIRGs, galaxies that exhibit high star formation (SF) rates, and host copious amounts of dust, supports this suggested bias. The transient Arp 299B-AT1 in the LIRG Arp 299 was shown to have arisen from a TDE based on the detection of a resolved and expanding off-axis radio jet (Mattila et al. 2018). The transient was only marginally detected in the optical, and as such was missed by optical surveys despite the distance of only ∼45 Mpc. Also, the serendipitous discovery of a TDE candidate in the LIRG IRAS F01004-2237 led Tadhunter et al. (2017) to suggest that LIRGs may have an elevated TDE rate, although the TDE nature of this transient is debated (Trakhtenbrot et al. 2019). Both of these events showed prominent and long-lasting IR emission, attributed to the absorption and re-radiation of the UV/optical light from the transient by the surrounding dust, with total radiated energies in the IR exceeding 10^{52} erg (Dou et al. 2017; Mattila et al. 2018). Although less energetic, such IR echoes have also been observed for a number of optically discovered TDEs (Dou et al. 2016; Jiang et al. 2016; van Velzen et al. 2016b).

A second phenomenon involving accretion by an SMBH that can result in large amplitude outbursts is observed in CLAGN. In the unified model, AGN are classified based on the presence of emission lines in their optical spectra, originating from the broad line region (BLR) close to the SMBH and narrow line region (NLR) further away. Type 1 AGN show both broad (typically full width at half-maximum (FWHM) of a few thousand km s^{-1}) and narrow (typically FWHM of a few hundred km s^{-1}) lines, whereas Type 2 show only narrow lines. This dichotomy is interpreted as a result of viewing angle, where in Type 2 the line of sight to the BLR is obscured by a dusty torus surrounding the AGN. In the case of CLAGN, the AGN type is observed to change between Type 1 and 2 or vice-versa in optical spectra. This phenomenon is poorly understood, but is commonly attributed to either a sudden change in accretion by the SMBH ionizing the BLR (e.g. MacLeod et al. 2016; Sheng et al. 2017), or variable obscuration, where dusty clouds passing across our line of sight cause the disappearance or appearance of broad emission lines (Goodrich 1989). The expected dynamical time-scales associated with variable obscuration are of the order of 10–70 yr (McElroy et al. 2016; Sheng et al. 2017), which excludes such CLAGN as an explanation for events on time-scales of a few years.

As TDE and CLAGN are both related to accretion by a central SMBH, there is a lack of clear observables to distinguish the two scenarios. It is even argued that CLAGN may be the direct result of TDEs (Eracleous et al. 1995; Merloni et al. 2015). Furthermore, observational biases likely affect our current understanding of these extreme and rare outbursts. Thus, careful study of individual nuclear events across multiple wavelengths is required (e.g. Mattila et al. 2018) to constrain their nature and establish observational tracers to aid future classification.

In this paper, we report the discovery and the multiwavelength follow-up campaign of AT 2017gbl, an extremely IR-bright transient coincident with the nucleus of the LIRG IRAS 23436+5257. The paper is organized as follows: Section 2 describes the discovery and follow-up campaign of AT 2017gbl, including the data reduction and photometry. Section 3 reports the analysis of the observed properties of AT 2017gbl and its host galaxy. This section includes SED fitting of the photometric data on the host and the transient, fitting of the spectral features, and analysis of the radio and X-ray properties. In Section 4, we discuss the key observations of the transient in the context of three different scenarios; an SN, a CLAGN, and a TDE. Finally, in Section 5 we present a summary of our findings. Throughout this paper we assume $H_0 = 70$ km s^{-1} Mpc^{-1}, $\Omega_\Lambda = 0.7$, and $\Omega_M = 0.3$.

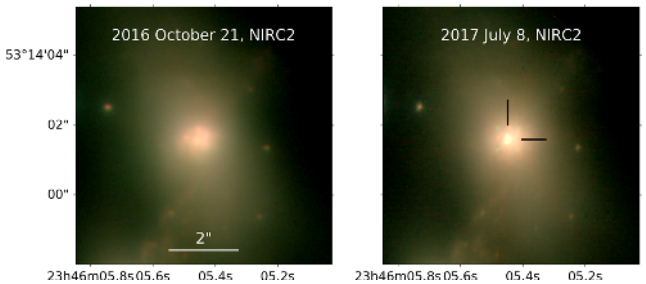

Figure 1. AT 2017gbl coincident with the Northern nucleus of IRAS 23436+5257, discovered with NIRC2. Left-hand panel shows a JHK_s colour composite from the NIRC2 template epoch in 2016 October. Right-hand panel shows a JHK_s colour-composite of the discovery epoch of AT 2017gbl in 2017 July. Image cutouts are ∼7.5 arcsec across.

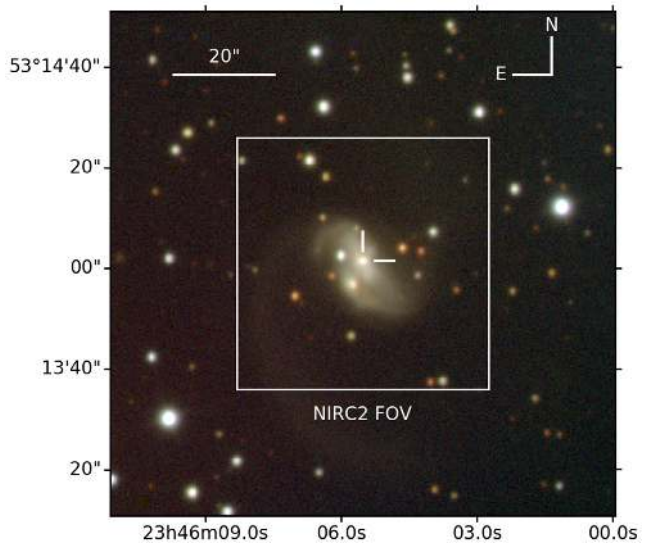

Figure 2. A *gri*-colour composite image of IRAS 23436+5257 as observed with ACAM on the WHT on 2017 July 10, three days after the discovery of AT 2017gbl. The transient was coincident with the Northern nucleus, indicated by tick marks. The FOV of the Keck NIRC2 discovery image is also shown. The ACAM image cutout shown here is 100 arcsec across.

2 OBSERVATIONS AND RESULTS

2.1 Discovery

AT 2017gbl was discovered as part of a systematic search for dust obscured SNe in the nuclear regions of LIRGs called project SUNBIRD (Supernovae UNmasked By Infra-Red Detection; Kool et al. 2018). The transient was discovered in IRAS 23436+5257 ($z = 0.034134$, Strauss et al. 1992, luminosity distance of 146 Mpc) in the near-IR K_s-band using Laser Guide Star Adaptive Optics (LGS-AO; Wizinowich et al. 2006) and the NIRC2 camera on the Keck II telescope on 2017 July 8.5 UT (MJD 57942.5; Kool et al. 2017); see Figs 1 and 2. Follow-up in *J*- and *H*-band was obtained

on the same night. Subtractions with *J*, *H*, and K_s observations from NIRC2 on 2016 October 21.4 UT showed an extremely bright residual coincident with the Northern nucleus of IRAS 23436+5257. Registering the image with 20 sources from the Pan-STARRS1 Data Release 1 archive (Chambers et al. 2016; Flewelling et al. 2016) yielded R.A. = $23^h46^m05.52^s$ and Decl. = $+53^\circ14'01.29''$, with 0.03 and 0.05 arcsec uncertainty in R.A. and Decl., respectively.

2.2 Near-IR and optical data reduction and photometry

Follow-up near-IR imaging of AT 2017gbl was obtained at an approximately monthly cadence with NOTCam on the Nordic Optical Telescope (NOT; Djupvik & Andersen 2010) by the NOT Unbiased Transient Survey (NUTS) collaboration,[1] from the discovery of the transient until the last detection in 2019 February, at +590 d after discovery. The transient was revisited with NIRC2 on Keck in K_s-band on 2017 December 5.2 UT, at +150 d. In the optical, AT 2017gbl was observed with ACAM on the William Herschel Telescope (WHT) in *g*, *r*, *i*, and *z* and with ALFOSC[2] on the NOT in *i* and *z*.

The NIRC2 and ACAM data were reduced using THELI (Erben et al. 2005; Schirmer 2013), following the steps outlined in Schirmer (2013) and Schirmer et al. (2015). THELI uses SCAMP (Bertin 2006) to calibrate the astrometry of the individual exposures to a reference catalogue to correct for image distortion before the final coaddition. The limited field of view (FOV) of NIRC2 did not contain enough 2MASS (Skrutskie et al. 2006) astrometric reference sources, so for the first NIRC2 epoch, image quality was optimized by calibrating the astrometry of the individual exposures to a catalogue extracted from a simple image stack of the same data set before coadding the resulting aligned exposures. Final astrometry was obtained by registering the coadded image to Pan-STARRS1 sources using IRAF[3] tasks. Subsequent NIRC2 images were calibrated using a catalogue extracted from the first K_s-band image. The NOTCam data were reduced using a version of the NOTCam QUICKLOOK v2.5 reduction package[4] with a few functional modifications (e.g. to increase the FOV of the reduced image).

Photometry of AT 2017gbl in the near-IR and optical images was carried out after image subtraction (e.g. Kool et al. 2018), using a slightly modified (to accept manual stamp selection) version of the image subtraction package ISIS 2.2 (Alard & Lupton 1998; Alard 2000). A NIRC2 image from 2016 October 21.5 UT, 260 d before discovery, was available as a transient-free reference image for the near-IR NIRC2 discovery image and the NIRC2 epoch at +150 d. However, due to the large difference in pixel scale and image quality between the NIRC2 reference image and the seeing-limited follow-up imaging with NOTCam, the NIRC2 template image was not suitable as a reference for NOTCam. Instead, reference NOTCam templates were obtained after the transient had faded below the detection limit, at epoch +744 d in *J* and *H* and at +798 d in K_s. In the optical, the WHT/ACAM observations from +570 d were used as transient-free reference images for the WHT/ACAM data. Similarly, ALFOSC imaging was obtained at +427 d to act as a reference for the optical NOT data.

Point-spread function (PSF) photometry of the transient was carried out using SNOOPY[5] from template subtracted images. The photometry of the transient in the seeing-limited near-IR (NOTCam) and optical (ALFOSC and ACAM) images were calibrated against five field stars from 2MASS and Pan-STARRS1, respectively. The photometry in the NIRC2 data was calibrated against five field stars in its small FOV, which in turn were calibrated with NOTCam imaging.

In case of a non-detection, a local detection threshold was determined by injecting sources of increasing brightness at the position of the transient, using the task *mkobjects* in IRAF, before performing image subtraction. The transient was considered recovered if the signal-to-noise ratio of the aperture flux at the position of the transient in the subtracted image was >5, compared to 24 empty positions in the immediate vicinity of the transient in the subtracted image.

The resulting host-subtracted light curve of AT 2017gbl in the optical and near-IR is shown in Fig. 3 and the photometry is listed in Tables A1 and A2, where the near-IR photometry is in the Vega system and the optical photometry in the AB system. The consistent evolution between the NIRC2 and NOTCam magnitudes supports the assumption that the NOTCam template epochs can be considered transient-free.

2.3 Mid-IR photometry

2.3.1 Spitzer

Follow-up imaging in the mid-IR was obtained with the *Spitzer Space Telescope* at 3.6 μm and 4.5 μm at seven different epochs, between 2017 November 13.1 UT at epoch +128 d and 2019 November 10.3 UT at epoch +855 d. Two archival epochs of the host galaxy were available from 2004 and 2011. The magnitude of the resolved Northern nucleus, host of AT 2017gbl, was determined at all epochs through relative photometry using a 3.8 arcsec aperture with five isolated field stars, for which magnitudes were based on catalogue fluxes from the *Spitzer* Heritage Archive. The *Spitzer* light curve of the Northern nucleus not only showed the brightening in the mid-IR due to AT 2017gbl, but also suggested evidence for a decline in magnitude between the two archival epochs from 2004 and 2011 of 0.1 ± 0.07 and 0.16 ± 0.08 magnitudes at 3.6 and 4.5 μm, respectively. The *Spitzer* magnitudes in the Vega system of the Northern nucleus of IRAS 23436+5257 are listed in Table A3 and the light curve is shown in Fig. 4.

2.3.2 WISE

In addition to *Spitzer*, archival observations from the Wide-field Infrared Survey Explorer (*WISE*) were available covering the pre-outburst host galaxy from 2010 until just after the 2016 near-IR reference epoch, as well as three post-outburst epochs.

WISE surveyed the full sky at 3.4, 4.6, 12, and 22 μm (channels *W*1–*W*4) in 2010 during its initial cryogenic mission, followed by the post-cryogenic and NEOWISE surveys in channels *W*1 and *W*2 upon depletion of its cryogen (Mainzer et al. 2011). The data from the initial and post-cryo missions have been made available as the AllWISE catalogue. Between 2011 February and 2013 October *WISE* was put in hibernation, after which it was reactivated for the

[1] http://csp2.lco.cl/not/

[2] The data presented here were obtained in part with ALFOSC, which is provided by the Instituto de Astrofisica de Andalucia (IAA-CSIC) under a joint agreement with the University of Copenhagen and NOTSA.

[3] IRAF is distributed by the National Optical Astronomy Observatory, which is operated by the Association of Universities for Research in Astronomy (AURA) under cooperative agreement with the National Science Foundation (Tody 1993)

[4] http://www.not.iac.es/instruments/notcam/guide/observe.html

[5] SNOOPY is a package for SN photometry using PSF fitting and/or template subtraction developed by E. Cappellaro. A package description can be found at http://sngroup.oapd.inaf.it/ecsnoopy.html

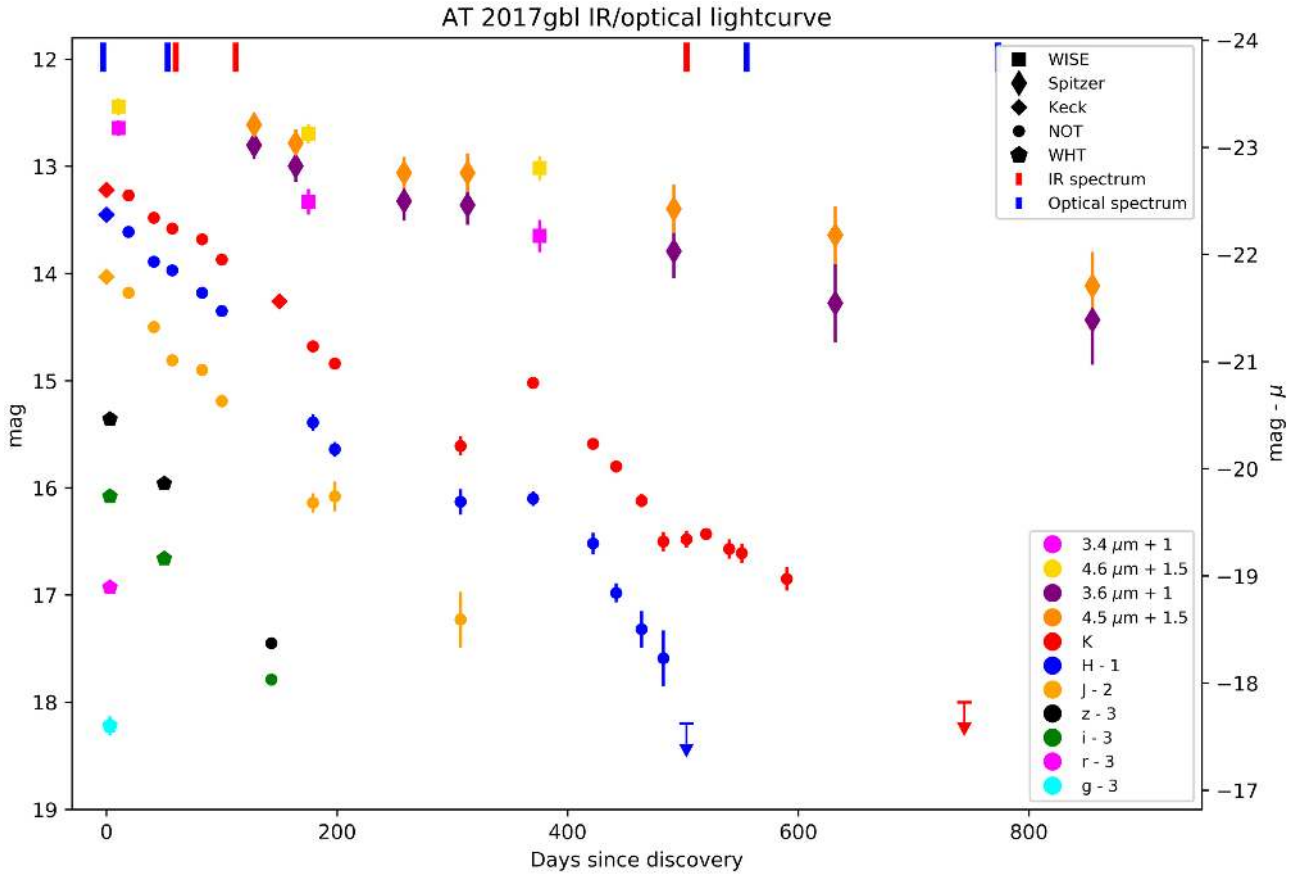

Figure 3. IR and optical evolution of AT 2017gbl. For clarity, the light curves have been offset as indicated in the figure legend. IR magnitudes are in the Vega system, optical magnitudes in the AB system. Pre-discovery non-detections are not shown, and consist of a JHK_s near-IR epoch at −260 d, and a 3.4/4.6 μm *WISE* epoch at −188 d.

NEOWISE Reactivation (NEOWISE-R; Mainzer et al. 2014) survey. In total IRAS 23436+5257 was observed twice during the cryogenic mission, once during the post-cryo mission and ten more epochs were obtained at regular intervals from 2013 until 2018 as part of the NEOWISE-R survey. Due to the observing strategy of *WISE*, each epoch consists of ∼12–18 exposures across ∼2 d, each with profile-fitted magnitudes reported in the AllWISE and NEOWISE-R catalogues. The host galaxy IRAS 23436+5257 consists of two nuclei, see Fig. 2, which were unresolved in the *WISE* data and well fit by a single profile with no deblending performed. In order to derive a single magnitude for each epoch, we averaged the magnitudes of all exposures of each epoch, after verifying no significant intraday variability occurred during an epoch, and excluding poor quality exposures (*qual_frame* > 0). The photometric *WISE* errors were taken as the standard error of the mean in each epoch and added in quadrature a flux error term of 2.4 and 2.8 per cent in *W*1 and *W*2, respectively, to reflect uncertainty between epochs (e.g. Jarrett et al. 2011). The *WISE* magnitudes in the Vega system of IRAS 23436+5257 at 3.4 and 4.6 μm are listed in Table A4 and the light curve shown in Fig. 4. As can be seen in the light curve, the pre-outburst *WISE* observations confirm the long-term decline in mid-IR of the host galaxy suggested by the archival *Spitzer* observations.

2.3.3 *Mid-IR photometry of AT 2017gbl*

The mid-IR light curves from both *Spitzer* and *WISE* clearly show that the system is not constant in flux, which means it is not appropriate to use a single pre-outburst epoch as a template for the image subtraction. Therefore the magnitude of AT 2017gbl in the mid-IR was determined by arithmetic magnitude subtraction, by subtracting the flux of a reference epoch from the post-outburst epochs. The mid-IR reference epoch was chosen to coincide with the near-IR reference epoch from 2016 October 21 in order to be able to construct a consistent host-subtracted spectral energy distribution (SED) of AT 2017gbl. Assuming any further decline of the host galaxy between the reference epoch and outburst epoch is similar in the near-IR and the mid-IR, this would affect the transient flux by a small constant offset across the SED.

The magnitude of the host galaxy in the *WISE* data at 2016 October 21.4 UT, −260 d before discovery, was determined by interpolating between the magnitudes of the 2016 July 17 and 2017 January 1 epochs. Using the *Spitzer* data, we established that all pre- and post-outburst variability of IRAS 23436+5257 originated in the Northern nucleus, by subtracting at each epoch the flux of the Northern nucleus from the flux in a larger aperture encompassing the full galaxy. The remainder, consisting of the flux of the Southern nucleus and faint structure between the nuclei, was constant within errors across all *Spitzer* epochs from 2004 until 2019. Therefore, we concluded that the residual flux after magnitude subtraction of the interpolated reference *WISE* epoch from the post-outburst *WISE* epochs can be fully attributed to AT 2017gbl.

The magnitude of the Northern nucleus of IRAS 23436+5257 in *Spitzer* bands at the time of the near-IR reference epoch was determined by subtracting the flux of AT 2017gbl from the 2017

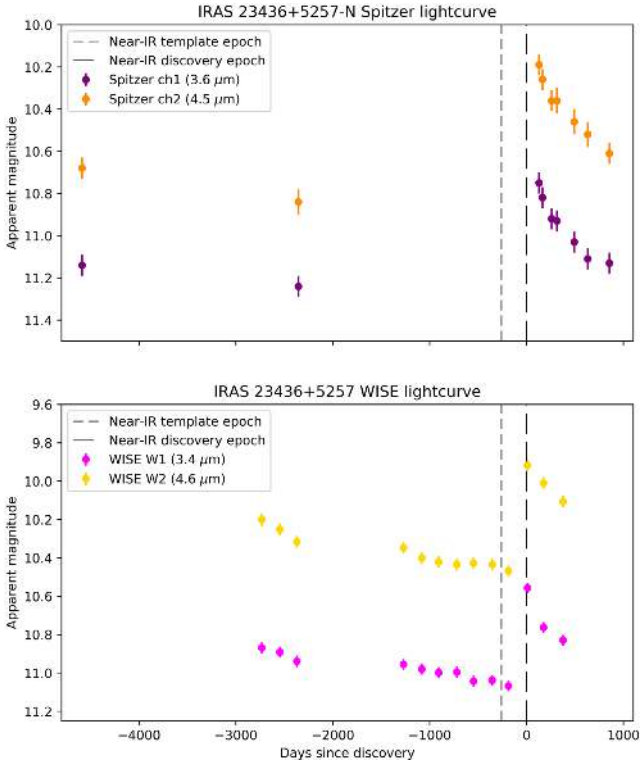

Figure 4. Top panel shows the *Spitzer* light curve at 3.6 and 4.5 μm of the Northern nucleus of IRAS 23436+5257. Bottom panel shows the archival *WISE* light curve at 3.4 and 4.6 μm of the full host galaxy. In the *Spitzer* data, the host nucleus of AT 2017gbl is resolved, whereas in the *WISE* data the host galaxy is not resolved. The vertical lines indicate the epochs of the near-IR reference data set (relevant for the construction of the SED of the transient, see Section 3.3.1) and the near-IR discovery epoch, respectively.

December 19 epoch, at +164 d. The flux of AT 2017gbl at 3.6 and 4.5 μm at 2017 December 19 was inferred from a blackbody, fitted to the (interpolated) *WISE* and near-IR K_s-band fluxes, see Section 3.3.1. The quiescent magnitude of the Northern nucleus of IRAS 23436+5257 derived in this way was magnitude subtracted from all post-outburst *Spitzer* observations to determine the magnitude of AT 2017gbl in the *Spitzer* data. Table A5 shows the mid-IR photometry of AT 2017gbl from the *Spitzer* and *WISE* observations, and the mid-IR light curve of AT 2017gbl is shown in Fig. 3. It must be noted that the arithmetic magnitude subtraction of the host introduces a systematic uncertainty related to the magnitude error of the template epoch, which is not included in the light curve or table. However, they are included in the SED fits of AT 2017gbl across all filters, discussed in Section 3.3.1.

2.4 Spectroscopy

2.4.1 Data reduction

Spectroscopic follow-up was performed in the optical with ALFOSC on the NOT and ISIS on the WHT, and in the near-IR with GNIRS on Gemini North and SpeX on IRTF. A log of the spectroscopic observations is reported in Table A6. All spectra will be made available via WISeREP (Yaron & Gal-Yam 2012). Here we briefly summarize the observations and data reduction steps for each data set.

The GNIRS cross-dispersed spectra were reduced using version 2.0 of the XDGNIRS[6] pipeline (Mason et al. 2015), which provides a convenient wrapper to a series of PyRAF tasks provided as part of the Gemini GNIRS data reduction package. Both epochs were observed in a similar manner, nodding the object on and off the 7 arcsec slit in an ABA pattern, with telluric reference stars (A0V spectral type) observed immediately before or after the object. The XDGNIRS pipeline was used to detect and trace the slit orders; extract the science and calibration data; apply the flat-field, spatial rectification, and wavelength calibrations; and correct the object spectra for telluric absorption. The latter was done accounting for intrinsic absorption features in the telluric reference star spectrum, and applying modest adaptive rescaling of the telluric spectrum to minimize the residual absorption residuals in the galaxy spectrum. Finally, aperture spectra were extracted using the APALL task to trace and sum a fixed aperture about the galaxy centre.

The ALFOSC spectra were reduced using the ALFOSCGUI package, which uses standard IRAF tasks to perform overscan, bias, and flat-field corrections as well as removal of cosmic ray artefacts using LACOSMIC (van Dokkum 2001). Extraction of the 1D spectra was performed with the APALL task and wavelength calibration was done by comparison with arc lamps and corrected if necessary by measurement of skylines. The spectra were flux calibrated against photometric standard stars observed on the same night.

The ISIS data were reduced with the same standard IRAF tasks and steps described above for ALFOSC.

The SpeX data were reduced using the publicly available SPEXTOOL software package (Cushing, Vacca & Rayner 2004). This reduction proceeded in a standard way, with image detrending, order identification, and sky subtraction. Corrections for telluric absorption utilized the XTELLCOR software and A0V star observations (Vacca, Cushing & Rayner 2003). After extraction and telluric correction, the 1D spectra from the six orders were rescaled and combined into a single spectrum.

2.4.2 Line identification

The near-IR spectra obtained with GNIRS are shown in Fig. 5. Both the near-IR spectra and the optical spectra (discussed below) have been corrected for Milky Way reddening (Schlafly & Finkbeiner 2011), adopting the Cardelli extinction law (Cardelli, Clayton & Mathis 1989) with $R_V = 3.1$. The GNIRS spectrum observed at +55 d after the discovery shows strong emission lines such as Paschen and Brackett recombination lines, He I, H_2, and [Fe II]. There are broad features visible in the Paschen and He I emission lines as well as broad emission features of O I at 8446 Å and 11 287 Å. These lines, particularly the 11 287 Å emission feature, indicate Bowen fluorescence where the O I 1025 Å transition is pumped by Lyman β emission, and cascades down through these lines (Bowen 1947). The spectrum obtained with the IRTF/SpeX two months later has much lower signal-to-noise. Of the broad features, only Paschen α is detected. The second GNIRS spectrum was obtained 448 d after the first one, +503 d after the discovery. During this period the transient decreased 2–2.5 mag in brightness in the near-IR. This dimming is visible in the spectra as a change in the shape of the continuum, which becomes less red as the transient has declined more in the redder bands. Additionally, the O I lines visible in the first GNIRS spectrum are no longer present in the second GNIRS spectrum and

[6] http://drforum.gemini.edu/topic/gnirs-xd-reduction-script

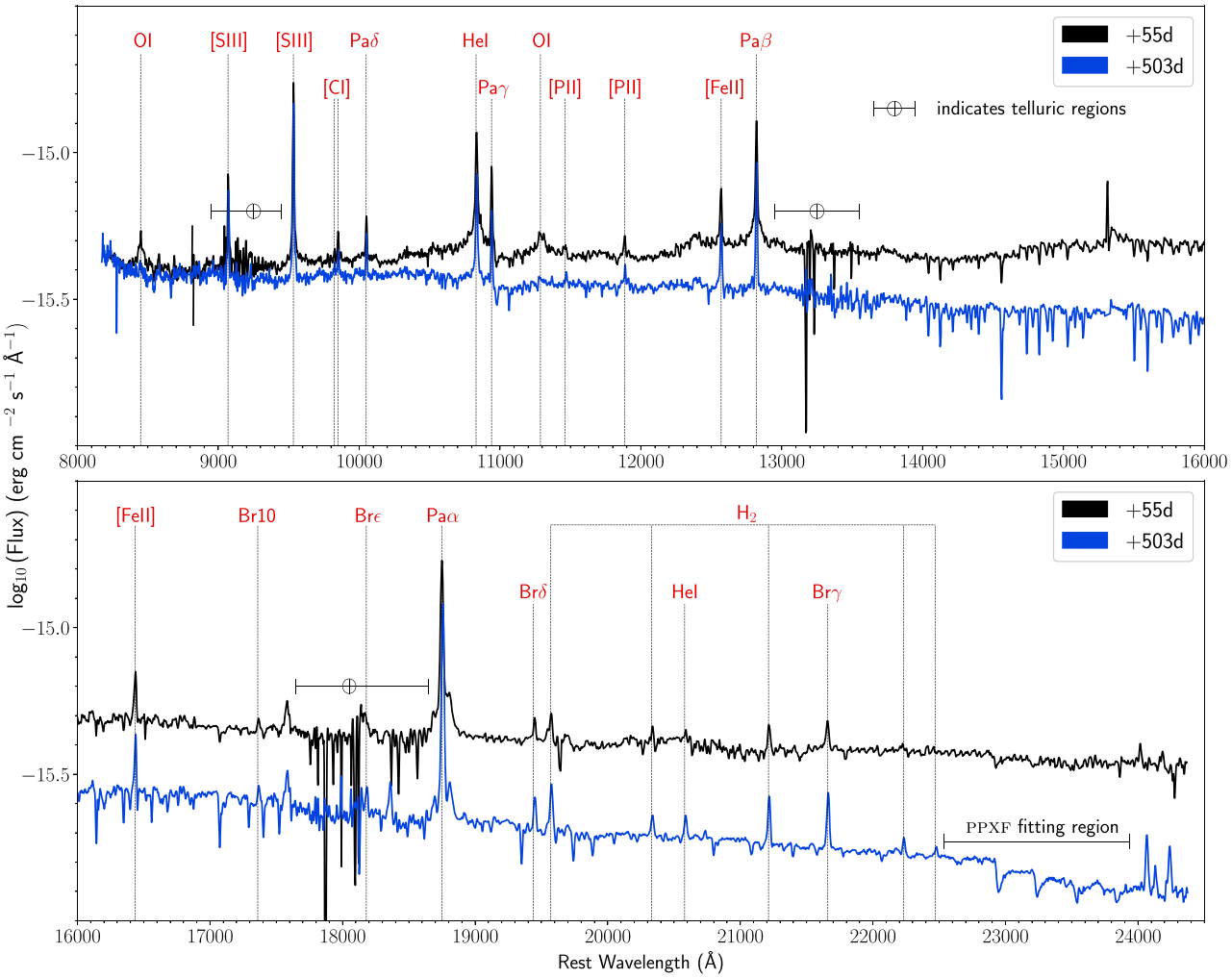

Figure 5. Near-IR follow-up spectra of AT 2017gbl from 2017 September 1 and 2018 November 23, taken with GNIRS. Spectra are corrected for Milky Way reddening. Prominent emission features are indicated. The region used to measure the velocity dispersion with PPXF fitting in Section 3.2.2 is marked.

the broad wings that were visible in the Paschen and helium emission lines have either disappeared or visibly decreased in strength.

The optical spectra obtained with ISIS and ALFOSC are shown in Fig. 6. The ISIS spectrum obtained +2 d after the discovery is dominated by narrow emission lines, such as H Balmer series, [O III], [N II], and [S II]. Additionally, the broad wings shown by the H α/[N II] complex give evidence for the presence of a broad emission line corresponding to H α. We also see the broad feature from O I λ8446. The ISIS spectrum obtained at +53 d shows little evolution in the narrow features but the broad features decrease in strength. The ALFOSC spectra obtained at +555 and +773 d continue to show little change in the narrow lines along with a reduction in the strength of the broad component of H α and no evidence for a broad feature from O I λ8446. We discuss the broad feature evolution in both optical and near-IR in Section 3.2.

Integral field spectroscopy of the Northern nucleus of IRAS 23436+5257 in the near-IR *K*-band is the only known pre-outburst spectrum available of the host galaxy. These data were serendipitously obtained with OSIRIS on the Keck telescope on 2016 November 18 as part of the Keck OSIRIS AO LIRGs Analysis Survey (U et al. 2019), one month after our near-IR imaging reference epoch and 1.5 months before the final pre-outburst epoch from *WISE*. We simulated the slit aperture used in the GNIRS spectra to obtain a 1D-spectrum in order to compare with the post-outburst GNIRS spectra. The OSIRIS spectrum showed narrow Brackett δ and γ in emission, with no sign of a broad component.

2.5 Radio observations

In the radio, we observed AT 2017gbl with milliarcsecond angular resolution using the Very Long Baseline Array (VLBA) at 4.4 and 7.6 GHz (simultaneously), and with the European Very long baseline interferometry Network (EVN) at 4.9 GHz, and with the Arcminute Microkelvin Imager Large Array (AMI-LA; Zwart et al. 2008; Hickish et al. 2018) at 15.5 GHz at a typical 40 arcsec×30 arcsec resolution. Our VLBA observations took place on 2017 August 15 (Perez-Torres et al. 2017) and 2017 October 20 at epochs +38 and +99 d, with clean beam major and minor axes of (4.5 × 1.3) milliarcsec^2 and (2.8 × 0.9) milliarcsec^2, respectively. Our EVN observations were carried out on 2019 February 15, at epoch +587 d, and resulted in an angular resolution of (9.3 × 4.6) milliarcsec^2. Three AMI epochs were obtained in the month following the discovery of AT 2017gbl, between 2017 July 12 and Aug 10 (Bright et al. 2017), and three more on a longer time-scale between +234 and +936 d after the discovery. We also retrieved a cutout at the position

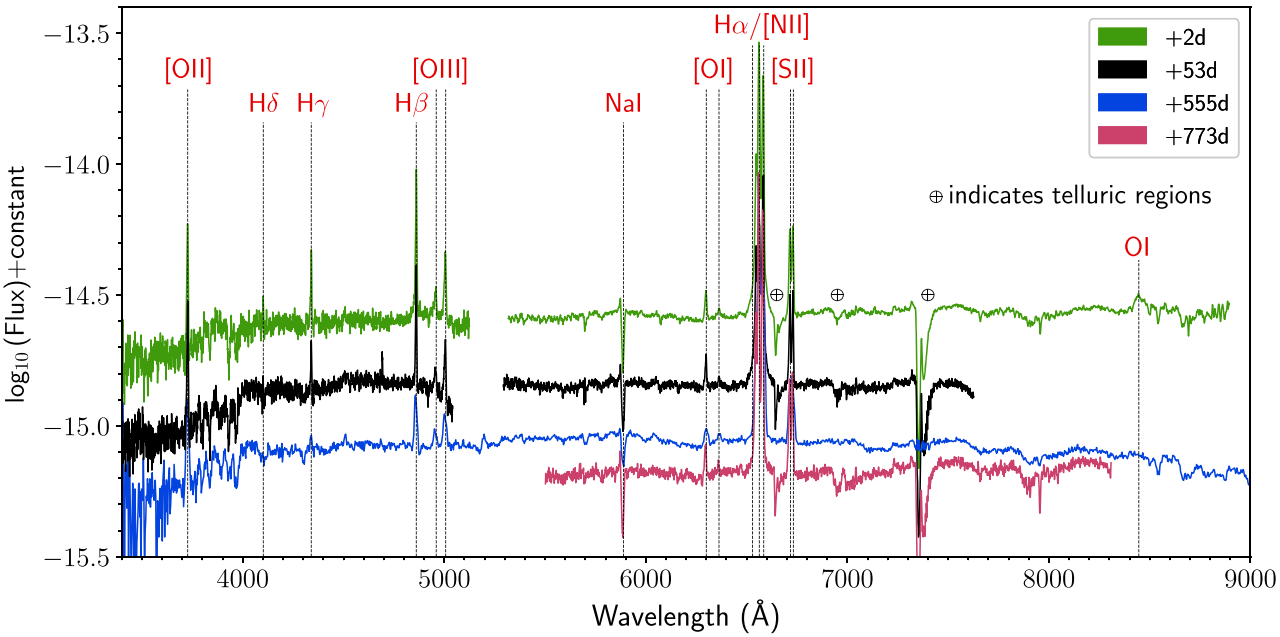

Figure 6. Optical follow-up spectra of AT 2017gbl. Spectra are corrected for Milky Way reddening. Some emission and absorption features are indicated. Note the broad O I feature at 8446 Å that is present initially but not in late observations. Note that the broadening of the narrow lines in the spectrum taken at +555 d is because the data are from a lower resolution instrument.

of the host from the VLA Sky Survey (VLASS; Lacy et al. 2020) at 3.0 GHz. This image was obtained on 2019 May 2 at epoch +663 d and has a resolution of $3\farcs1 \times 2\farcs2$.

We carried out our VLBA observations recording at a bit rate of 2 Gbps using dual polarization, and made use of the wide *C*-band receiver, so we simultaneously observed our target at the central frequencies of 4.4 and 7.6 GHz, with a bandwidth of 128 MHz at each sub-band. We used 1 MHz width channels and an integration time of 2 s, which resulted in negligible time- and band-width smearing. We followed standard calibration and imaging procedures within the AIPS package. We used the compact, nearby VLBA calibrator J 2353+5518 as the phase-reference source. Our VLBA observations from +38 d showed one unresolved source within the 1 arcsec by 1 arcsec FOV at R.A. = $23^{h}46^{m}05.5173^{s}$ and Decl. = $+53^{\circ}14'01.260''$, and the astrometric uncertainty in that position is less than 1 milliarcsecond at both frequencies. Those coordinates are only 0.04 arcsec from the transient position in the near-IR, and are well within the near-IR astrometric uncertainties. The second VLBA epoch at +99 d showed a significant increase in flux at 4.4 and 7.6 GHz, as well as a change in the spectral index.

We scheduled our EVN observations similarly to our VLBA observations, and used seven antennas of the Western EVN array at a data rate of 2 Gbps using dual polarization in eight sub-bands of 32 MHz each. We reduced the data following standard procedures for the EVN, and took into account ionospheric corrections for each antenna. We also performed two self-calibration steps (first in phase only and then in amplitude and phase) on the phase reference source (J 2353+5518) to correct the antenna gains in the different sub-bands. This correction was especially needed for the data of a couple of antennas that had no system temperature measurements. The calibrator J 2353+5518 has a compact morphology and a flux density of 0.47 ± 0.04 Jy at 4.9 GHz. With 64 channels per sub-band and an integration time of 2 s, the FOV was limited by time- and bandwidth-smearing to ∼45 arcsec. A map centred on the Southern nucleus, which is only ∼5 arcsec away from the Northern nucleus, yields no detections. In the Northern nucleus we detected an unresolved source at a position coincident with the coordinates reported based on the VLBA observations. The EVN observation at +587 d showed that the source was still unresolved, but its 4.9 GHz flux density had decreased, compared to the early 4.4 GHz VLBA observations.

The AMI observations were taken at a central frequency of 15.5 GHz over a 5 GHz bandwidth covered by 4096 channels and measures I+Q polarization. The array has baselines between 18 and 110 m leading to a characteristic resolution of between 30 arcsec and 50 arcsec depending on the number of antennas and the sky position of the target. Observations lasted between 3 and 4 h, yielding r.m.s. values between 41 and 57 μJy beam^{-1}. The phase calibrator J2355+4950 was observed interleaved with the target field for ∼100 s for each ∼10 min on source, and either 3C 286 or 3C 48 was used as the absolute flux calibrator. Data were calibrated and imaged in the quick look format, where data are averaged into eight frequency channels of 0.625 GHz width at the correlator, and then flagged for radio frequency interference, and flux and phase calibrated using the custom reduction pipeline for quick look data REDUCE_DC (e.g. Perrott et al. 2015; Bright et al. 2018). Data were then imported into CASA and further flagging was performed and the data were imaged using standard imaging techniques with a clean gain of 0.1 and manual masking. Fluxes were extracted using the CASA task IMFIT. The source was point like (unresolved) in all the observations and we did not fix the dimensions of the synthesized beam when fitting. The source peaked in flux density around the epoch +21 d, after which the source declined in flux up to the epoch +848 d. Between the final two epochs at +848 and +936 d no variability is observed in flux density within 1-σ. We, therefore, consider these two epochs to be transient-free, tracing the quiescent flux from the host galaxy and its Southern companion at 15.5 GHz.

2.5.1 *Host contamination correction*

We list in Table A7 the properties of the pre- and post-outburst radio observations. We note that the measurements from all these observations include a contribution from the host. In the case of the AMI observations the measurements are also contaminated by emission from the Southern nucleus, which clearly emits in the radio as seen in the VLASS cutout. To alleviate this contamination, we looked for available pre-outburst radio images. The host was within the surveyed area of the NRAO VLA Sky Survey (NVSS; Condon et al. 1998) with a resolution of (45 × 45) arcsec^2 at 1.4 GHz. In the extracted NVSS cutout we find that IRAS 23436+5257 is a compact source with a flux density of 18.70 ± 1.85 mJy, where we have considered a 3 per cent uncertainty in the flux calibration (Condon et al. 1998), that we added in quadrature to the r.m.s. to obtain the total uncertainty in the flux density. The quiescent flux of IRAS 23436+5257 at 15.5 GHz, taken as the mean value of the AMI epochs of +848 and +936 d, is 3.60 ± 0.18 mJy. The angular resolution of AMI and NVSS are comparable, and therefore we can assume that they are tracing the emission of the same region. In this way, we obtained a two-point spectral index between 1.4 and 15.5 GHz of $\alpha = -0.69 \pm 0.05$ ($S_\nu \propto \nu^\alpha$) for IRAS 23436+5257 in its quiescent state. This spectral index agrees well with the expected value for star-forming galaxies at $z < 2$ (Delhaize et al. 2017). Therefore, most of the flux density seen by the low-resolution radio observations of AMI and the NVSS likely comes from extended, large-scale star-formation in the host. Using the spectral index between 1.4 and 15.5 GHz, we obtain a flux density of the host at 3.0 GHz of 11.09 ± 1.02 mJy. Having the contribution of the host to the total emission at 3.0 and 15.5 GHz, we subtracted it from the total flux densities to obtain the radio flux densities from the AMI and VLA observations that correspond to AT 2017gbl. The VLBA and the EVN observations at milliarcsecond angular resolution trace the flux density from the innermost nuclear regions hosting AT 2017gbl. We assume that the transient dominates the compact radio emission traced by the VLBA and the EVN. The resulting transient fluxes are listed in column (7) of Table A7, and shown in Fig. 7.

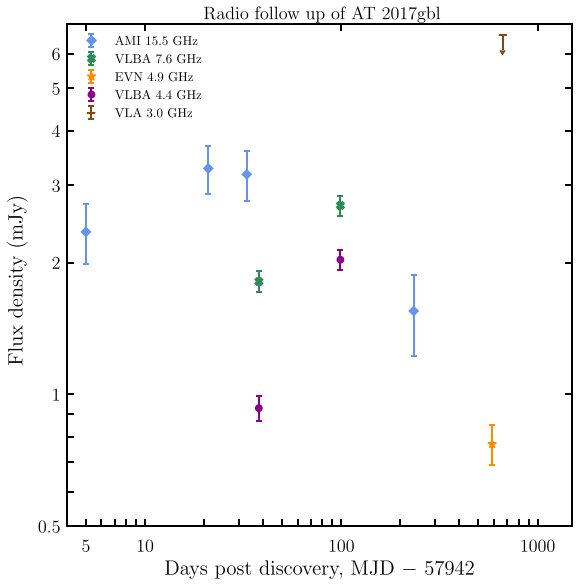

Figure 7. Radio light curve of AT 2017gbl. The flux densities from AMI and the VLA have been corrected for host galaxy contributions. The AMI epochs of +848 and +936 d are not shown here, as they are considered transient-free and act as the quiescent level of the host galaxy at 15.5 GHz (see the text for details). The epoch at 3 GHz with the VLA has a large uncertainty, and we show the 3σ upper limit here instead of the host-subtracted value.

2.6 X-ray observations

In X-rays we first observed the transient as a target-of-opportunity (ToO) on 2017 September 13 for 3 ks with the X-ray telescope on board *the Neil Gehrels Swift observatory* (ObsID 00010290001). No source was found with a 3σ luminosity upper limit of 4.7×10^{41} erg s^{-1} in the 0.2–10 keV energy band, measured using an absorbed power-law model with $N_{\rm H} = 3.0 \times 10^{21}$ cm^{-2} and a photon index 0.9 (see below). A second, deeper X-ray observation with a 10 ks exposure was obtained through Director's Discretionary Time with the ACIS-S imager on *Chandra X-ray Observatory*, on 2017 November 3, +118 d after the discovery. In the *Chandra* observation (ObsID 20831) a point source coincident with the transient's position was detected, see Fig. 8. The offset between the position of AT 2017gbl and the centroid position of this source is ∼0.4 arcsec, which is less than the typical celestial location accuracy of *Chandra*.[7]

A spectrum of the source was extracted from the *Chandra* observation with the SPECEXTRACT tool from the CIAO 4.10 software-package, using a 2.5 arcsec aperture (containing ∼95 per cent of emission from the on-axis source) positioned on the source centroid.

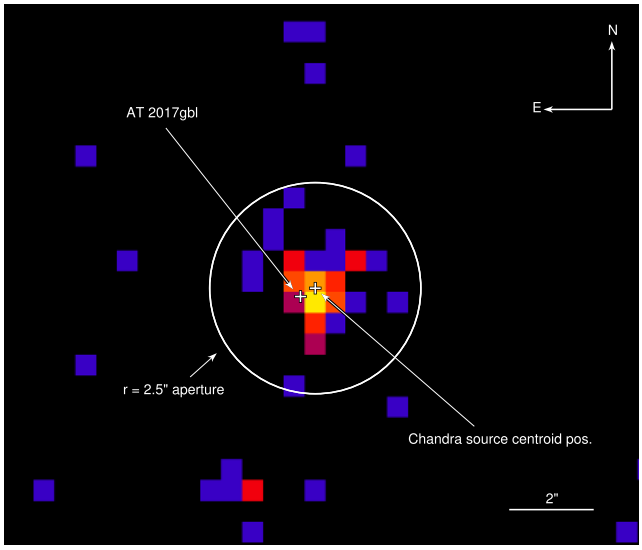

Figure 8. X-ray image of AT 2017gbl obtained with *Chandra* in 0.5–7 keV band. The circle represents a 2.5 arcsec aperture centred on the X-ray source containing ∼95 per cent of emission from the on-axis source, which was used to extract the spectrum shown in Fig. 9. The position of the centroid and the position of AT 2017gbl as observed in the near-IR are also indicated.

As any X-ray emission from a possible AGN in the nucleus would be almost entirely absorbed in the *Chandra* energy band, we assume that the observed X-ray flux primarily originates from the circumnuclear population of X-ray binaries (XRBs). To test if the X-ray source can be explained by emission originating in the host galaxy of AT 2017gbl we therefore adopt a simple absorbed power-law model to represent the combined XRB population (e.g. Mitsuda et al. 1984). To improve our fit, we also restrict the number of free parameters in our model by

[7]For details, see https://cxc.harvard.edu/proposer/POG/html/chap5.html#tth_sEc5.4

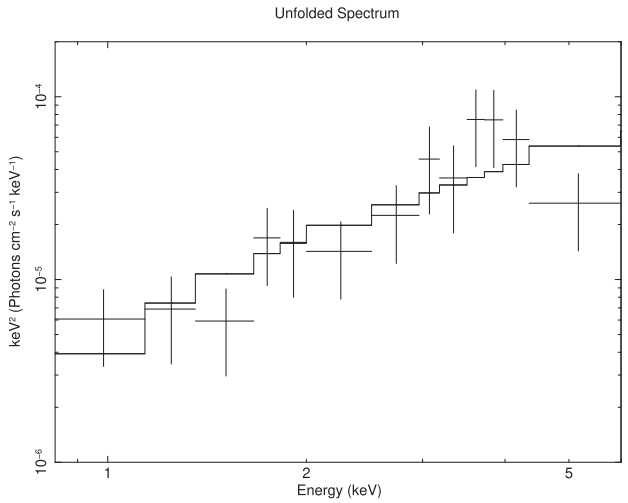

Figure 9. *Chandra* X-ray spectrum of the source fitted with an absorbed power law where $N_H = 3.0 \times 10^{21}$ cm^{-2} and the fitted photon index is ∼0.9.

adopting $N_{\rm H} = 3.0 \times 10^{21}$ cm^{-2} from Mineo, Gilfanov & Sunyaev (2012),[8] to estimate the average $N_{\rm H}$ value outside of the nucleus. In Section 3.5, we will discuss our results in the context of the empirical relationship between the star formation rate and the X-ray luminosity of a LIRG's XRB-population established in Mineo et al. (2012), and by adopting the same value for absorption, our model will better align with theirs.[9] We therefore only fit the powerlaw photon-index, using XSPEC 12.10.0c. For the photon-index, we obtain the best fit of 0.9 ± 0.3, and for the power law component the unabsorbed model flux of $1.2 \pm 0.2 \times 10^{-13}$ erg cm^{-2} s^{-1} (0.5–8.0 keV), see Fig. 9. This corresponds to an unabsorbed X-ray luminosity of $L_{\rm X} = 3.2^{+0.6}_{-0.5} \times 10^{41}$ erg s^{-1}.

3 ANALYSIS

3.1 Host galaxy SED fitting

IRAS 23436+5257 is a bright LIRG with an IR luminosity of $L_{\rm IR} \sim 4 \times 10^{11}$ L$_\odot$ (Sanders et al. 2003; adjusted to $H_0 = 70$ km s^{-1} Mpc^{-1}). This LIRG was included in the SUNBIRD sample because the expected core-collapse SN (CCSN) rate inferred from its $L_{\rm IR}$ (Mattila & Meikle 2001) is as high as ∼1 yr^{-1}. This empirical relation, however, assumes a negligible contribution to the IR luminosity of the galaxy from a potential AGN. There has not been any evidence in the literature of the presence of an AGN in IRAS 23436+5257, based on hard X-ray (14–195 keV) observations (Koss et al. 2013), equivalent width of the PAH feature (Yamada et al. 2013), or mid-IR *W*1–*W*2 colours from *WISE* (Assef et al. 2018a).

However, the long-term pre-outburst variability in the mid-IR (see Fig. 4) hints at the presence of an obscured AGN in the host galaxy of AT 2017gbl, as AGNs are known to show such low-amplitude smooth variability in the mid-IR (Kozłowski et al. 2016).

In order to determine the different components contributing to the total luminosity of IRAS 23436+5257, we modelled its multi-wavelength SED with a combination of libraries of starburst, AGN torus, AGN polar dust, and spheroidal/cirrus component models. For this purpose, we collected photometric data points available from the literature ranging from the optical to the submillimetre, from Pan-STARRS1, 2MASS, *Spitzer*/IRAC, IRAS (Sanders et al. 2003), *ISO* (Stickel et al. 2004), and GOALS (Armus et al. 2009; Chu et al. 2017). In addition, we included mid-IR spectra in the range between 5 and 37 microns observed with the *Spitzer* IRS instrument and available through the Combined Atlas of Sources with *Spitzer* IRS Spectra. These observations and their reductions are described by Lebouteiller et al. (2011). The spectral resolution of the IRS data was reduced to better match the resolution of the radiative transfer models and have a wavelength grid that is separated in steps of 0.05 in the log of rest wavelength. However, in order to better constrain the AGN and starburst contributions to the SED more points were included around the 9.7 μm silicate feature and the PAH features. We note that no scaling was required between the photometric points from the different sources and the mid-IR spectra which we take as an indication that the emission is dominated by one of the two galaxies.

In particular, we used the library of starburst models computed with the method of Efstathiou, Rowan-Robinson & Siebenmorgen (2000) as revised by Efstathiou & Siebenmorgen (2009), and the library of AGN torus models computed with the method of Efstathiou & Rowan-Robinson (1995). The polar dust model was calculated in a similar way as in Mattila et al. (2018). We assume the polar dust is concentrated in discrete optically thick ($\tau_{\rm V} \sim 100$) clouds which are assumed to be spherical with no internal heating source. For each of these clouds, we carry out a radiative transfer calculation to calculate their emission using the code of Efstathiou & Rowan-Robinson (1995) and assuming a normal interstellar dust mixture. However, we assume a fixed temperature of 1300 K for the dust which in this simple model is assumed to be determined by the external illumination of the clouds by the transient event. The library of spheroidal models was as described in Herrero-Illana et al. (2017). More details of the method will be given in Efstathiou et al. (2020, in preparation). The SED fits were carried out with the MCMC SED fitting code SATMC (Johnson et al. 2013).

Fig. 10 shows the best fitting SED model for IRAS 23436+5257 before and 10 d after the discovery of the outburst, composed of a starburst, an AGN torus, a spheroidal host, and a polar dust component at 1300 K. The pre-outburst model is fitted to fluxes at epochs preceding AT 2017gbl. The post-outburst fit is based on the same data with the addition of the observed fluxes of AT 2017gbl in the optical, near-IR, and mid-IR (0.5–4.6 μm range). We do not expect any significant emission from the transient at longer wavelengths and assume that the archival pre-outburst flux densities describe the SED adequately at wavelengths > 5 μm, similar to the case of Arp 299-B AT1 (Mattila et al. 2018). All model parameters were fixed to values within a range of 1 per cent from the pre-outburst fit, with the exception of the polar dust temperature that was fixed to 1300 K and luminosity which was left as a free parameter. The resulting model fitting parameters and the derived physical quantities are listed in Table 1.

It is noteworthy in particular that the model requires a significant AGN contribution of 32 ± 2 per cent to the total luminosity of the galaxy, after correcting the AGN torus luminosity for anisotropic emission. Attempts to model the data without an AGN component resulted in poorer fits (maximum log-likelihood < −3300 versus −1166) that did not recover well the spectral range between 3 and 40 μm around the 9.7 μm silicate absorption feature. In the case of the fit including an AGN we have a total of 13 free parameters and 30 degrees of freedom whereas in the case of the fit without an AGN the number of free parameters is 8 resulting in 35 degrees of

[8]We note that the Galactic $N_{\rm H}$ in the direction of AT 2017gbl is 1.86×10^{21} cm^{-2} (HI4PI Collaboration 2016).

[9]Minor variations in the $N_{\rm H}$ value do not have a significant effect on our analysis.

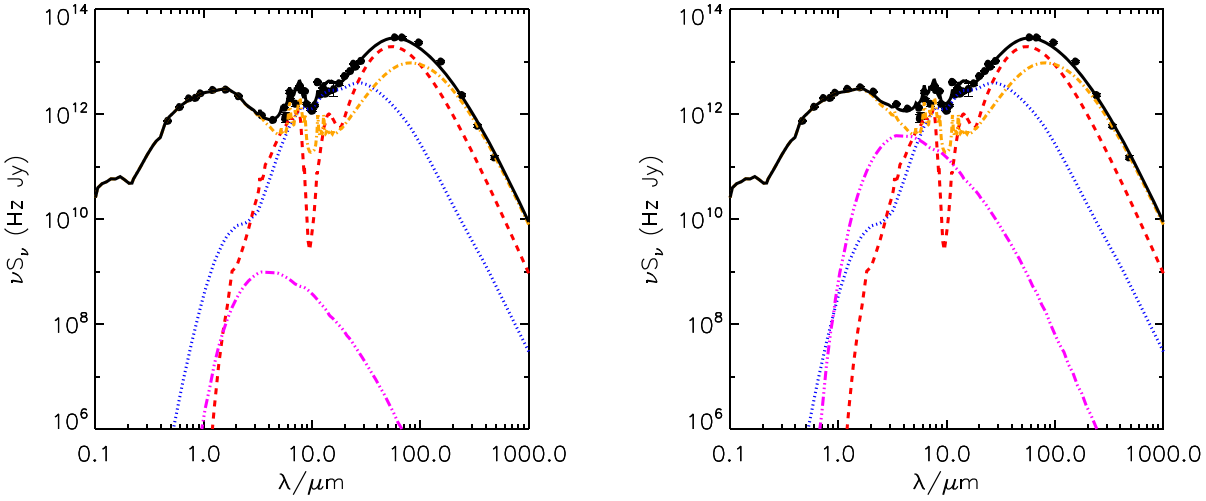

Figure 10. The best fitting SED model for IRAS 23436+5257 obtained using the MCMC code SATMC (Johnson et al. 2013), pre-outburst on the left and post-outburst (+10 d) on the right with the contribution from AT 2017gbl included at the wavelength range 0.5–4.6 μm. The flux measurements are indicated by the black dots, and the model SED is composed of a starburst (red), an AGN torus (blue), a spheroidal host (orange), and a polar dust at 1300 K (magenta) component.

Table 1. The model parameters obtained when fitting the SED of IRAS 23436+5257 along with the derived bolometric luminosities. In the post-outburst case all the parameters were fixed to the pre-outburst values within a range of 1 percent, with the exception of the polar dust temperature and luminosity. The CCSN and SF rates are calculated based on the fitted mode parameters. The SF rate is averaged over the past 50 Myr. The SF rate averaged over the age of the starburst is higher by about a factor of 3.

	Pre	Post
Total luminosity (10^{11} $L_\odot$)	$4.35^{+0.09}_{-0.08}$	$4.35^{+0.09}_{-0.08}$
Starburst luminosity (10^{11} $L_\odot$)	$1.61^{+0.04}_{-0.10}$	$1.61^{+0.04}_{-0.10}$
Spheroidal luminosity (10^{11} $L_\odot$)	$1.34^{+0.10}_{-0.04}$	$1.33^{+0.10}_{-0.04}$
AGN luminosity (10^{11} $L_\odot$)	$1.40^{+0.09}_{-0.09}$	$1.40^{+0.09}_{-0.09}$
Polar dust luminosity (10^{9} $L_\odot$)	$0.01^{+0.12}_{-0.006}$	$3.8^{+0.2}_{-0.2}$
Polar dust covering factor (per cent)	$0.01^{+0.17}_{-0.01}$	
Core-collapse supernova rate (SN yr^{-1})	$0.16^{+0.01}_{-0.01}$	
SF rate, averaged over the past 50 Myr ($M_\odot$ yr^{-1})	$14.9^{+1.6}_{-1.2}$	

freedom. Given the small difference in the degrees of freedom the difference in log-likelihood is significant favouring the presence of an obscured AGN.

Based on this result, we inspected the *Spitzer* IRS spectrum at the original resolution for the mid-IR high ionization fine structure lines that are strong in AGN, such as [NeV] 14.3 μm and [OIV] 25.9 μm. We do not find evidence for these lines, which is in agreement with the previous results of Inami et al. (2013), who did not detect these lines at 3σ significance in their study which included this spectrum. While the presence of strong [NeV] and [OIV] lines signifies an AGN, their absence does not exclude the presence of an obscured AGN significantly contributing to the IR luminosity, as shown in the sample of LIRGs optically classified as Seyfert 2 galaxies presented by Alonso-Herrero et al. (2012). Due to the inclination of the torus in our model for IRAS 23436+5257, the apparent AGN luminosity is lower by a factor of ∼2.4, which may explain why an AGN was not detected by previous studies.

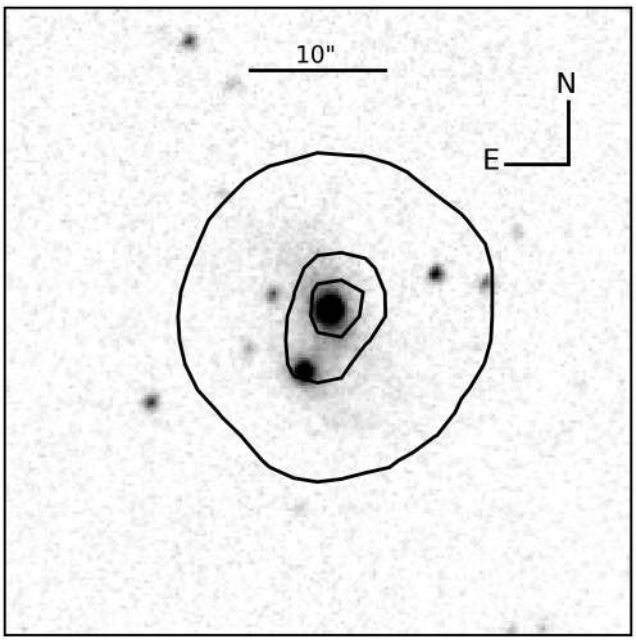

Figure 11. NOT K_s-band image of IRAS 23436+5257 from 2017 July 27 with 24 μm MIPS contours overplotted. The 24 μm emission is concentrated on the Northern nucleus, supporting it as a potential AGN host.

IRAS 23436+5257 consists of two nuclei, and the model fit is based on flux densities for the whole galaxy in which the two nuclei are not resolved. In order to determine the host nucleus of the possible AGN, we compare contours from a 24 μm MIPS image with a near-IR K_s-band NOT image in Fig. 11. As shown, most of the 24 μm emission from IRAS 23436+5257 originates in the Northern nucleus. Based on Fig. 10, the AGN component should dominate the emission at 24 μm which would originate from a region a few hundred pc or less in size (e.g. Lopez-Rodriguez et al. 2018). Therefore we conclude that the Northern nucleus is a potential host to a dust-obscured AGN.

As a result of the contribution to the IR luminosity by the AGN, the expected CCSN rate of IRAS 23436+5257 derived from the SED fitting is much lower, at $0.16 \pm 0.01\,\mathrm{yr}^{-1}$, than expected from its IR luminosity L_{IR}. Additionally, the data are best fit by a model where the torus obscures a direct line of sight to the central AGN. The optical depth along the line of sight of the best-fitting model is $\tau \sim 90$ at 1 μm, equivalent to an extinction of $A_{\mathrm{V}} \sim 300$ mag. This extinction would fully obscure the central engine at optical, near- and mid-IR wavelengths. Assuming a standard conversion to hydrogen column density from Predehl & Schmitt (1995), this A_{V} corresponds to $N_{\mathrm{H}} \sim 5.4 \times 10^{23}\,\mathrm{cm}^{-2}$, which should be considered as a lower limit for the actual column density given the dust evaporation in the innermost regions close to the AGN. This corresponds to values expected from a Compton-thick AGN.

3.1.1 *Pre-outburst mid-IR variability*

The presence of a dust-obscured AGN in IRAS 23436+5257 would explain the low-amplitude mid-IR variability observed before the discovery of AT 2017gbl. As seen in Fig. 4, the variability in the mid-IR shown by the Northern nucleus of IRAS 23436+5257 can be divided into two stages: a long-term decline spanning >10 yr, followed by the steep increase and subsequent decline related to AT 2017gbl. The long-term decline as shown in the *WISE* data prior to the outburst amounts to 0.20 ± 0.04 and 0.27 ± 0.05 mag at 3.4 and 4.6 μm, respectively, over the course of ∼2500 d, or 7 yr. Galaxies hosting an AGN have been observed to show mid-IR variability that typically has a lower amplitude and a longer time-scale than in the optical (e.g. Glass 2004). This difference is because the variations in the mid-IR originate in a region of a much larger extent than the optical light, and as a result any short time-scale variations are smoothed out. Normal mid-IR AGN variability has been quantified by Kozłowski et al. (2016) to be <0.3 mag over 7 yr, which agrees well with the observed smooth pre-outburst mid-IR decline of the Northern nucleus of IRAS 23436+5257. The mid-IR variability connected to AT 2017gbl consists of an increase of 0.51 ± 0.04 and 0.55 ± 0.04 mag at 3.4 and 4.6 μm, respectively, between the last pre-outburst and the first post-outburst NEOWISE-R epochs. This increase over ≤198 d is not possible to reconcile with 'normal' AGN variability.

3.2 Optical and near-IR spectral analysis

In our spectra of AT 2017gbl, we see narrow unresolved emission lines in the optical and near-IR associated with hydrogen, helium, [O III], [N II], and H_2, which are commonly found within star-forming LIRGs (Burston, Ward & Davies 2001; Valdés et al. 2005). Given the evidence for an obscured AGN from the SED fitting of IRAS 23436+5257, we search for signs of this also in the spectra. We do not see any high ionization coronal lines such as [Ca VIII] λ23218, [Si VI] λ19620, or [S VIII] λ9915, which would indicate the presence of strong X-ray flux associated with an AGN. The near-IR galaxy spectral surveys of Riffel, Rodríguez-Ardila & Pastoriza (2006), Riffel et al. (2019) show that none of the narrow lines we detect can unambiguously indicate the presence of an AGN, as they are often found in LIRGs with no evidence for an AGN.

A common criterion for assessing the relative contributions of an AGN and star formation is the BPT diagram (Baldwin, Phillips & Terlevich 1981). For IRAS 23436+5257 we measure $\log_{10}([\mathrm{O\,III}]/\mathrm{H}\beta) = -0.11 \pm 0.16$ and $\log_{10}([\mathrm{N\,II}]/\mathrm{H}\alpha) = -0.128 \pm 0.09$ which places this galaxy in the composite AGN + SF region, as shown in Fig. 12. Based on the position on the BPT diagram, the presence of an AGN cannot be confirmed nor ruled out. Larkin et al. (1998) suggested the line ratios [Fe II]/Pa β and H_2/Br γ as a diagnostic of whether galaxies are LINERs or Seyfert type AGNs using the near-IR spectral region, and this idea was further developed in Rodríguez-Ardila et al. (2004), Rodríguez-Ardila, Riffel & Pastoriza (2005), Riffel et al. (2013), and Väisänen et al. (2017). Riffel et al. (2013) find $0.6 <$ [Fe II] / Pa $\beta < 2$ and $0.4 < H_2$ / Br$\gamma < 6$ as determining criteria for an AGN classification based on a large sample of objects, with lower values for these ratios indicating a star-forming galaxy (SFG). In our +503 d spectrum of the Northern nucleus of IRAS 23436+5257, we find [Fe II] / Pa $\beta = 0.47 \pm 0.02$ and H_2 / Br$\gamma = 0.80 \pm 0.03$, placing it within the SFG region for the former value, and AGN region for the latter. These ratios cannot provide us with a clear indication of an AGN, and again suggests that the Northern nucleus of IRAS 23436+5257 is a transitional object. Lamperti et al. (2017) find in their survey that these diagnostics are often not sufficient to diagnose AGN, as SFGs can fulfill both criteria.

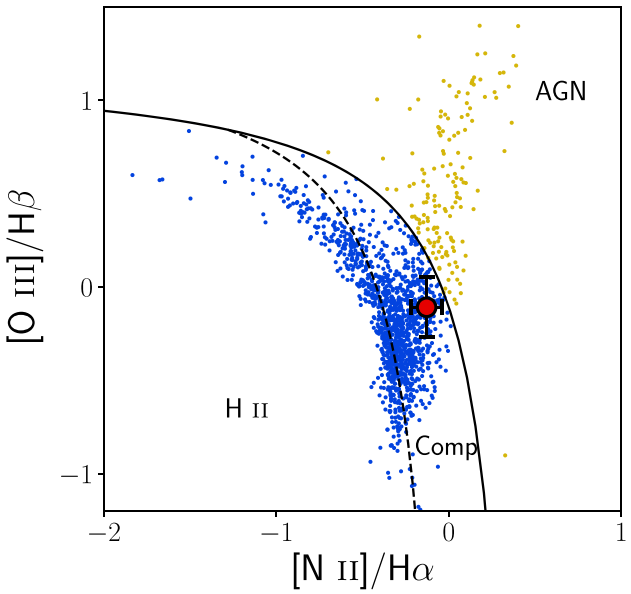

Figure 12. BPT diagram showing the position of IRAS 23436+5257 with a red point. The galaxy data shown is taken from SDSS DR7 (Abazajian et al. 2009), regions indicated are taken from Kewley et al. (2006). Colouring of points indicates the region they lie within, not an independent determination of their type. Code distributed as part of ASTROML (Vanderplas et al. 2012) was adapted to generate this plot.

3.2.1 *Emission line fitting*

In order to quantify the widths and the apparent evolution of the broad velocity components visible in the strong emission lines such as Paschen α and He I, we simultaneously fit the lines with a broad and a narrow Gaussian, while linearly fitting the local continuum. Measurements are corrected for instrumental broadening, the resolving powers (R) of the observations are listed in Table A6. The fitting results are shown in Table 2, with the fits to Paschen α and He I λ10830 shown in Fig. 13. The line fluxes of all the broad line profile components decreased significantly between the early and late GNIRS epochs, and as such it is natural to relate this to the transient

Table 2. Emission line widths and fluxes. Where no value is given, the line was not detected. FWHM are corrected for instrumental broadening. Uncertainties listed in the table are statistical and derived from the covariance matrix of the fitting parameters. There is an additional ∼15 percent uncertainty in the flux measurements coming from the absolute flux calibration of the spectra, that is not included in the listed uncertainties. Note that we chose not to simultaneously fit regions where multiple broad features were blended, such as Paschen γ, δ, and He I, with multiple Gaussians and thus consider the fits in these regions to be less reliable.

Emission line	Epoch d	Narrow line FWHM km s^{-1}	Broad line FWHM km s^{-1}	Narrow line flux 10^{-15} erg cm^{-2} s^{-1}	Broad line flux 10^{-15} erg cm^{-2} s^{-1}
Paschen α	+55	220 ± 12	2110 ± 120	23.3 ± 0.8	26.2 ± 2.2
	+503	200 ± 6	2070 ± 140	19.2 ± 0.3	8.5 ± 0.9
Paschen β	+55	189 ± 7	1840 ± 60	8.7 ± 0.2	10.4 ± 0.6
	+503	191 ± 6	–	7.6 ± 0.1	–
Paschen γ	+55	200 ± 25	–	4.5 ± 0.3	–
	+503	175 ± 25	–	3.0 ± 0.2	–
Paschen δ	+55	190 ± 40	2800 ± 600	1.6 ± 0.2	1.9 ± 0.6
	+503	160 ± 40	–	1.4 ± 0.2	–
Brackett γ	+55	190 ± 50	1600 ± 400	2.1 ± 0.3	1.6 ± 0.6
	+503	201 ± 27	–	2.4 ± 0.2	–
He I λ10830	+55	319 ± 14	2440 ± 130	8.2 ± 0.3	13.3 ± 1.0
	+503	262 ± 14	1910 ± 210	5.5 ± 0.2	3.8 ± 0.7
O I λ8446	+55	–	1640 ± 140	–	3.4 ± 0.4
	+503	–	–		–
O I λ11287	+55	–	1930 ± 100	–	5.2 ± 0.4
	+503	–	–	–	–

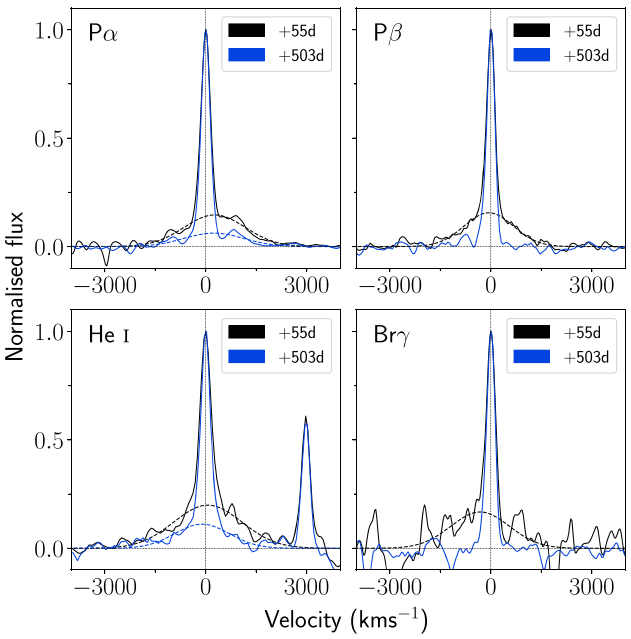

Figure 13. Fits to the emission lines that show more prominent broad features in our GNIRS spectra. The peak of the narrow feature is normalized to 1. The dashed lines show the broad Gaussians that were fitted to the spectra to derive the values listed in Table 2.

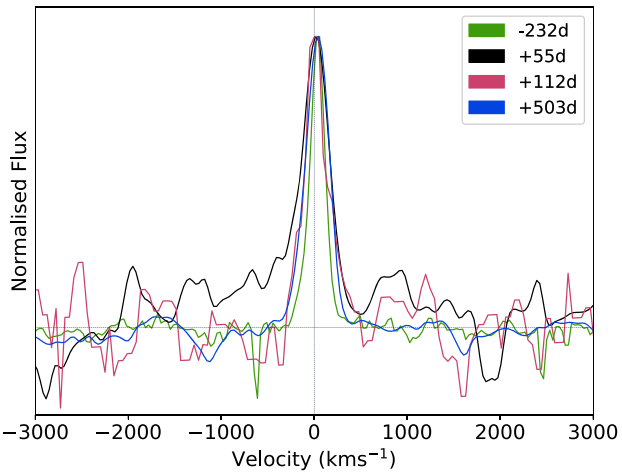

Figure 14. Comparison of the Br γ emission line evolution over time. The spectral peaks have been normalized to one after subtraction of a linear fit to the continuum. The only spectrum that shows evidence for a broad component is at +55 d (black line).

event. The detection of a broad component in both Paschen α and β allows us to determine the line-of-sight extinction affecting the broad line emission, by comparing the ratio to the theoretical value assuming Case B recombination (Osterbrock 1989; Gaskell 2017). Adopting the Cardelli extinction law (Cardelli et al. 1989) with $R_V = 3.1$, this ratio implies 2.5 ± 0.6 mag of host galaxy extinction in V-band, where the uncertainty is derived from the co-variance matrix for the least-squares fit. It is interesting to note that this value is a couple of orders of magnitude lower than estimated towards the potential AGN in Section 3.1, implying that the broad emission lines would not originate directly from regions close to the central engine. Alternatively, the lines we observe could be scattered into our line of sight by electrons and dust in the polar regions after being produced close to the SMBH. This phenomenon has been observed in other AGN such as the well-known NGC 1068 (Antonucci & Miller 1985).

We inspect the evolution of the Br γ emission line profile using the OSIRIS spectrum that was taken 232 d before AT 2017gbl was discovered. In Fig. 14 we show the evolution of this line. There is no

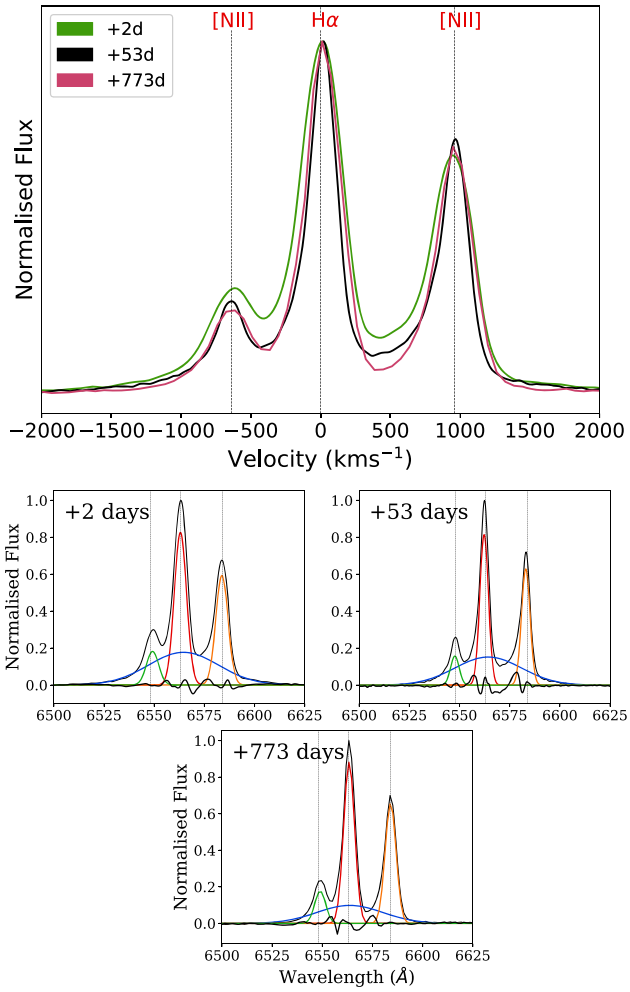

Figure 15. Upper panel: Comparison of the H α region in our optical spectra. The peak of the H α line was normalized to one, after subtraction of a linear background. The earliest spectrum has a stronger contribution from the broad component than the two later observations. Lower panel: Multicomponent fitting of the features in the H α region. Data are shown in black, and fit residuals are shown along the *x*-axis.

evidence for a broad emission line component in the spectrum taken before the transient's discovery nor in the spectra taken at +112 d and +503 d, but the spectrum from +55 d does show a broad component. This gives a pre-explosion limit of −232 d for the appearance of this line, which is similar to the −260 d implied by the near-IR light curve.

We show the region around H α in Fig. 15, with the emission line profile normalized with respect to the peak of H α. The earliest spectrum, obtained a few days after the discovery shows evidence for an underlying broad H α feature. This feature appears to have very rapidly declined in flux, with the spectrum taken at +53 d already appearing similar to a spectrum taken 2 yr afterwards. Also in Fig. 15, we show emission line fits to the spectra. Three narrow components with equal FWHM were simultaneously fitted to the data, along with a broad component. The values derived from these fits are listed in Table 3. We find that all the spectra show some evidence for a broad component, with a similar FWHM of ∼1800 km s^{-1}. There is no statistically significant evidence for variability in the narrow emission lines between these spectra.

Table 3. Emission line widths obtained from the fits to the optical spectra. The narrow line FWHM refers to the emission lines used for the H α and [N II] lines which were kept at the same width, and the broad line width refers to the broad H α emission feature. The velocity given for the narrow lines is with respect to the H α rest wavelength. The narrow lines are not resolved in the observations at +2 and +773 d, all other lines are corrected for instrumental broadening. Uncertainties are derived from the covariance matrix of the fitting parameters.

Epoch Days	Narrow line FWHM km s^{-1}	Broad line FWHM km s^{-1}
+2	327.4 ± 1.7	1951 ± 20
+53	162.1 ± 2.1	1898 ± 26
+773	293.1 ± 3.6	1790 ± 100

3.2.2 *Velocity dispersion measurements*

In order to make a measurement of the mass of the SMBH hosted by the northern nucleus of IRAS 23436+5257, we make use of the Penalised Pixel Fitting (PPXF) routine (Cappellari 2017) to measure the stellar line-of-sight velocity distribution (LOSVD) from absorption lines in our spectra. To measure the LOSVD, template stellar spectra are convolved with the corresponding LOSVD, which is parametrized by a series of Gauss–Hermite polynomials. More details can be obtained in Cappellari & Emsellem (2004) and Cappellari (2017).

We chose to fit the region from 23 300–24 750 Å in the observer frame which contains the CO absorption band heads (indicated in Fig. 5). This was performed in the GNIRS spectrum from +503 d, as the CO features have high signal to noise and are well resolved at the resolving power $R \sim 1300$ of GNIRS with our instrument setup. The aperture extracted is 0.9 arcsec wide, corresponding to ∼640 pc at the distance of this galaxy. We made use of templates from the Gemini Near-IR Late-type stellar library (Winge, Riffel & Storchi-Bergmann 2009), which contains spectra of this wavelength region for 60 stars with spectral types ranging from F7 III to M5 III obtained at spectral resolution of ∼3.2 Å (FWHM). Before fitting, the template spectra are degraded to the resolution of the GNIRS spectrum. We allowed the fitting routine to include a multiplicative and an additive order one Legendre polynomial in the fit, to account for continuum emission arising from the galaxy and the contribution from the transient that is still present at this time. Otherwise, we made use of the default software parameters and in particular the bias, which controls the extent that the higher order Hermite polynomials affect the fit, was left at the default. Given the systematic sources of uncertainty we list below, this choice will not be a dominating source of uncertainty in our measurements.

The fit results in a LOSVD of $\sigma = 81 \pm 15$ km s^{-1}. We make use of the scaling relation given by equation 7 of Kormendy & Ho (2013) to derive a BH mass of $\log_{10}(M_{BH}) = 6.8 \pm 0.4\,M_{\odot}$. This relationship has an intrinsic scatter in $\log(M_{BH})$ of 0.29 ± 0.03. Note that this relation is poorly calibrated for galaxies with $\sigma <$ 100 km s^{-1}, as there are only a few such galaxies in the sample used to derive it. Furthermore other authors (e.g. Rothberg & Fischer 2010; Riffel et al. 2015) have noted that the value of σ measured using the CO bandheads is systematically lower than that measured with the Ca near-IR triplet, in particular for LIRGs. Riffel et al. (2015) find a mean logarithmic offset of −0.29 ± 0.12 for the measured M_{BH} of spiral galaxies from the CO lines, compared to those measured with the Ca lines. As we cannot measure the LOSVD from the Ca near-IR triplet in our spectra due to noise, we apply this correction to the BH mass. We prefer this to the relationship

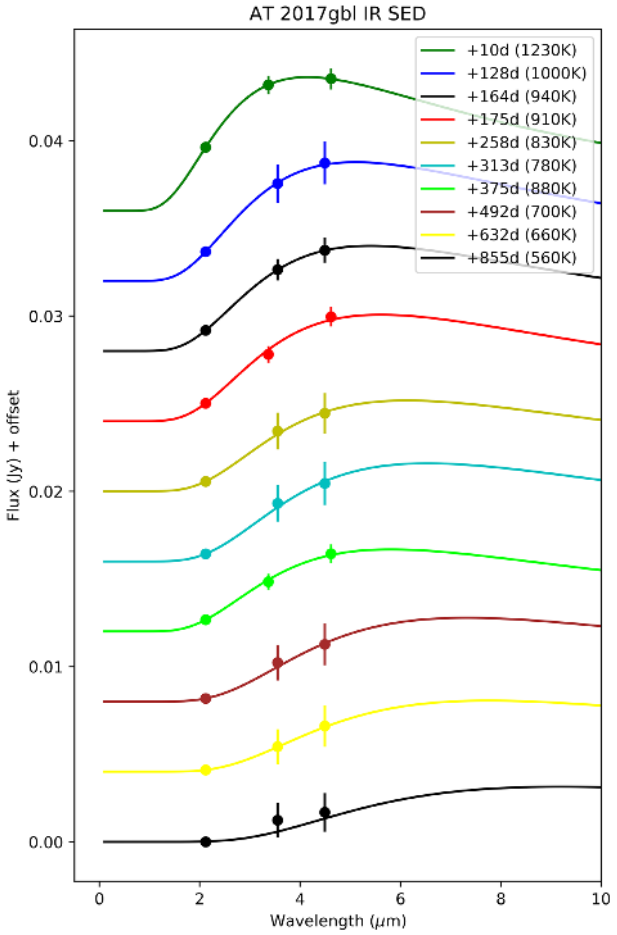

Figure 16. Blackbody fits of the mid-IR and interpolated near-IR K_s-band fluxes at the mid-IR epochs. Epochs are offset for clarity, and labelled by days since discovery. Fitted blackbody temperatures are given in parentheses.

derived in Rothberg & Fischer (2010) for LIRGs, as they derived this exclusively from post merger, single nuclei LIRGs, whereas IRAS 23436+5257 is still a double nuclei system. Applying this correction, we find a BH mass of $\log_{10}(M_{BH}) = 7.1 \pm 0.4\,M_{\odot}$. Using this value for the BH mass and the value for the AGN luminosity given by our SED fitting, we can derive an Eddington ratio of $\epsilon = 0.35 \pm 0.32$. The implications of the BH mass will be discussed in Section 4.

3.3 Transient SED fit

3.3.1 Single IR component

From the light curve of AT 2017gbl, it is clear the transient is growing redder over time, declining slowly in the mid-IR and more rapidly in the near-IR. The evolution of the IR SED is well fitted by a single warm blackbody component with a decreasing blackbody temperature and increasing radius, see Fig. 16. In this figure the SEDs of the transient are shown at the epochs of the mid-IR observations, with the K_s measurements from NOTCam and NIRC2 interpolated to the mid-IR epochs. Overplotted are single blackbodies fitted to the near-IR K_s-band and the two mid-IR bands from either *Spitzer* or *WISE*. The near-IR J and H-bands were not included in the fit, since a second optical blackbody component likely contributes significant flux at these wavelengths, see Section 3.3.4. The blackbody parameters were estimated using the EMCEE PYTHON implementation of the Markov chain Monte Carlo method (MCMC; Foreman-Mackey et al. 2013). The *Spitzer* epoch of +632 d was fitted to the mid-IR fluxes and a K_s-band flux extrapolated from the final four K_s-band detections. The *Spitzer* epoch of +855 d was fitted to the mid-IR fluxes and a K_s-band flux of zero, with an uncertainty consistent with the upper limit of $K_s > 18.0$ from the +726 d near-IR epoch.

The fitted blackbody parameters are listed in Table 4, given by the median value of the posterior distributions of blackbody radius and temperature realizations from the MCMC fitting, with 1σ errors. Blackbody radius and temperature evolution is shown in the left-hand panel of Fig. 17. As the host-subtracted transient source grows fainter in flux, the uncertainties in flux increase, resulting in the increasing uncertainties of the fitted blackbody parameters. We note that for the epoch of +10 d the temperature estimated from the simple blackbody fit of 1230 ± 20 K agrees within the uncertainties with the temperature estimated from the full radiative transfer model for the polar dust component at the same epoch of 1300 K. This gives confidence that the parameters obtained by fitting a simple blackbody function to the observed SED give a reasonable description of the properties of the IR emitting region.

Table 4 also lists the luminosity in erg s^{-1} associated with the blackbody using the Stefan–Boltzmann law:

$$L = 4\pi R^2 \sigma T^4, \quad (1)$$

where R is the radius of the blackbody in cm, T its temperature in Kelvin, and σ the Stefan–Boltzmann constant (5.670×10^{-5} erg cm^{-2} s^{-1} K^{-4}). The total energy of AT 2017gbl radiated in the IR can be estimated by integrating the luminosity over the time between the epochs. As shown in in Table 4 and the right-hand panel of Fig. 17, the radiation emitted as a blackbody between +10 and +855 d after

Table 4. Blackbody parameters obtained for the 2.2–4.5 μm SEDs of AT 2017gbl.

UT Date	MJD	Epoch (d)	Radius (10^{-2} pc)	Temperature (K)	Luminosity (10^{43} erg s^{-1})	Cumulative radiated energy (10^{50} erg)
2017-07-18.3	57952.3	+10	3.8 ± 0.2	1230 ± 20	2.3 ± 0.3	–
2017-11-13.1	58070.1	+128	4.9 ± 0.5	1000 ± 30	1.6 ± 0.4	2.0 ± 0.3
2017-12-19.8	58106.8	+164	5.1 ± 0.4	940 ± 20	1.4 ± 0.2	2.5 ± 0.3
2017-12-30.0	58117.0	+175	5.4 ± 0.3	910 ± 20	1.3 ± 0.2	2.6 ± 0.3
2018-03-23.5	58200.5	+258	5.7 ± 0.9	830 ± 30	1.0 ± 0.3	3.5 ± 0.3
2018-05-17.1	58255.1	+313	6.5 ± 1.0	780 ± 30	1.1 ± 0.4	3.9 ± 0.4
2018-07-18.6	58317.6	+375	5.0 ± 0.4	880 ± 20	1.0 ± 0.2	4.5 ± 0.4
2018-11-12.6	58434.6	+492	7.1 ± 1.6	700 ± 30	0.8 ± 0.4	5.4 ± 0.5
2019-04-01.5	58574.5	+635	7.1 ± 2.1	660 ± 40	0.6 ± 0.4	6.3 ± 0.7
2019-11-10.3	58797.3	+855	8.1 ± 3.9	560 ± 60	0.4 ± 0.4	7.3 ± 1.0

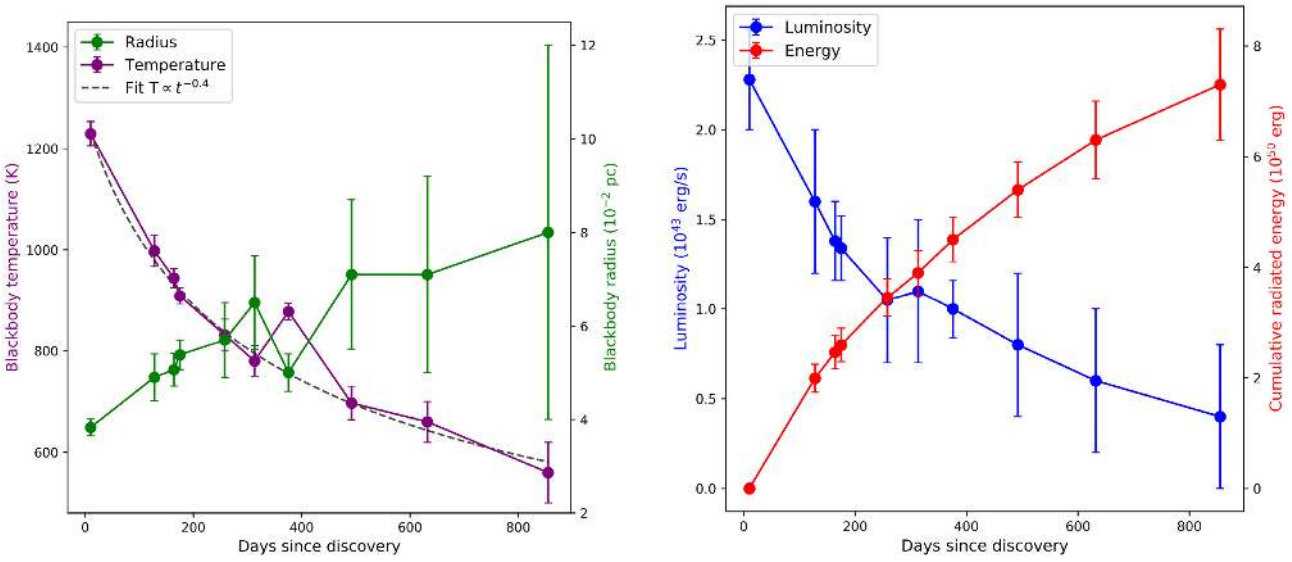

Figure 17. Left-hand panel: evolution of the IR blackbody parameters. Right-hand panel: IR blackbody luminosity and the cumulative radiated energy.

discovery totals $7.3 \pm 1.0 \times 10^{50}$ erg. This value is a lower limit for the total radiated energy, since the transient was discovered after (or at) the peak, and the transient was still faint but ongoing at +855 d, so the rise to the peak and the late time evolution are not included, and neither is the contribution of a potential cooler component at longer IR wavelengths. The implications of the energy budget of AT 2017gbl on its nature are discussed in Section 4.

3.3.2 IR echo

There has been considerable research in recent years on the variability of extragalactic sources in the mid-IR, made possible to a large extent by the observing strategy and sampling of the AllWISE and NEOWISE-R surveys, as exemplified in Fig. 4. These studies have resulted in the discovery of multiple mid-IR outbursts with some similarities to AT 2017gbl (Dou et al. 2016, 2017; Jiang et al. 2016; van Velzen et al. 2016b; Jiang et al. 2017; Assef et al. 2018b; Mattila et al. 2018; Wang et al. 2018; Gromadzki et al. 2019; Jiang et al. 2019; Yan et al. 2019; Yang et al. 2019; Sun et al. 2020), which have been interpreted as thermal emission of dust following absorption of a fraction of the UV/optical light from an energetic transient event. Such 'IR echoes' have often been shown to be well described by a single component blackbody with temperatures ranging from ∼500 K to ∼1500 K, with the upper limit being dictated by the temperature at which dust sublimates (e.g. Draine & Lee 1984). A sufficiently energetic optical outburst will sublimate the dust out to a radius which depends on the peak luminosity of the outburst (Koshida et al. 2014). As a consequence, the IR emission will only start rising after a time delay, and the IR peak is delayed with respect to the optical peak. The luminosity and time-scale of an IR echo depends on the luminosity of the event, the dust geometry, and on the dust covering factor, i.e. the fraction of UV-optical radiation from the event intercepted by dust in the surrounding few parsecs (Lu, Kumar & Evans 2016).

As the IR fluxes of AT 2017gbl are well fitted with a single component blackbody throughout its evolution, with the temperature decreasing from 1230 K down to 560 K, these IR fluxes are consistent with being dominated by an IR echo following the event's UV/optical display. We note that at the epoch of +375 d the blackbody parameters in Fig. 17 show a break in their trend. This is related to the bump in the near-IR light curve observed at +370 d, see Fig. 3. This could be the result of an influx of UV/optical continuum photons from a secondary outburst following the main outburst. We further discuss this bump in the context of the nature of AT 2017gbl in Section 4.

3.3.3 Implications of IR echo properties

The IR echo is a response to the underlying transient event, and as such its properties can be linked to that of the transient by making some basic assumptions. We assume a spherically symmetric system where a short pulse of bolometric luminosity $L_{\rm bol}$ is generated from the outburst at $t = 0$. As a result of intensive heating, dust particles will sublimate within certain radius $R_{\rm sub}$ where the dust is heated to the sublimation temperature $T_{\rm sub} \simeq 1600$ K (the exact value depends mildly on the grain composition and size, e.g. Lu et al. 2016). Beyond the sublimation radius, the temperature T of a grain of radius a at radius R from the source is determined by the equilibrium between heating and radiative cooling:

$$e^{-\tau}\frac{L_{\rm bol}}{4\pi R^2}\pi a^2 Q_{\rm abs} = \langle Q_{\rm abs}\rangle_{\rm P}\, 4\pi a^2 \sigma T^4. \quad (2)$$

Here $Q_{\rm abs} \simeq 1$ is the absorption efficiency factor of the incident radiation (Draine 2011) and $\langle Q_{\rm abs}\rangle_{\rm P}$ is the Planck-averaged absorption efficiency factor (Draine & Lee 1984). Although dust grains are efficient absorbers of UV/optical photons, the absorption (and hence emission) efficiency drops as the photon wavelength becomes comparable or smaller than the grain size. For the range of temperatures $500 \lesssim T \lesssim 1500$ K and dust radii $a \lesssim 1\,\mu$m, we take the approximation $\langle Q_{\rm abs}\rangle_{\rm P} \simeq a_\mu (T/1000\,{\rm K})$ (where $a_\mu = a/(\mu{\rm m})$) appropriate for graphite grains.[10] For the astrophysical silicate model, the approximation is $\langle Q_{\rm abs}\rangle_{\rm P} \simeq 0.3 a_\mu$ without the temperature dependence.

[10]Optical properties of interstellar dust grain models have been calculated by Draine & Lee (1984), and the tabulated data can be found at https://www.astro.princeton.edu/draine/dust/dust.html

The factor $e^{-\tau}$ accounts for the flux attenuation by the surviving dust below radius R. If the system is optically thin for UV/optical photons, then this factor can be ignored. In the other extreme limit where the reprocessing system is highly optically thick, then all the UV/optical photons from the central explosion are absorbed in a thin layer just beyond the sublimation radius. The IR echo of AT 2017gbl with temperature $T \in (500, 1200)$K comes from radii that are a factor of $(T_{\rm sub}/T)^{2.5} \gtrsim 2$ larger than the sublimation radius. Dust particles at these radii are heated by the re-emitted IR photons from the UV-absorbing layers. We infer from the H recombination lines that the reprocessing system is optically thin to IR photons, so the $e^{-\tau}$ can also be ignored. The only difference from the UV optically thin case is that the bolometric luminosity $L_{\rm bol}$ should be understood as the IR emission near the sublimation radius, which may be a factor of a few less than the original UV/optical luminosity due to smearing on a time-scale of $R_{\rm sub}/c \lesssim 100$ d (as we show below).

In the following, we adopt $R = ct$ and ignore the $e^{-\tau}$ factor based on the above argument. Taking graphite grain as our fiducial model, equation (2) can be rewritten as:

$$T^5 = \frac{L_{\rm bol}}{a_\mu} \frac{1000K}{16\pi\sigma c^2} \frac{1}{t^2}. \quad (3)$$

This relation means that $T \propto At^{-0.4}$ where A is a constant:

$$A = \left(\frac{L_{\rm bol}}{a_\mu} \frac{1000K}{16\pi\sigma c^2} \right)^{1/5}. \quad (4)$$

As the UV/optical radiation propagates outwards with time, the temperature of the dust re-emitted IR emission drops with time as a power law. Since $t = t_{\rm epoch} - t_0$ is the time since the outburst, this allows us to determine the outburst epoch t_0. In Fig. 17 is shown the result from fitting $T = A\,t^{-0.4}$ to the observed blackbody temperature evolution using EMCEE, with the normalization factor A and t_0 as free parameters. We do not include the epoch at +375 d in the fit, since this bump is likely due to extra emission of hotter dust on the opposite side from the observer with longer light-path than ct (basically breakdown of our spherical assumption) or a secondary outburst from the continuum source. We note that fitting the temperature evolution only before the bump gives the same result as the complete fit shown here.

The resulting best estimate of t_0 is 142 ± 11 d. Furthermore, the fitted value of A allows us to estimate $L_{\rm bol}/a_\mu$, resulting in $L_{\rm bol}/a_\mu = 1.2 \pm 0.1 \times 10^{45}$ erg s^{-1}. The range for the grain radius a is typically 0.1−1 μm, so $L_{\rm bol} \sim 0.1 - 1 \times 10^{45}$ erg s^{-1}. The determination of t_0 and $L_{\rm bol}$ assumed the outburst to be well described as a short pulse of constant luminosity, while in reality the outburst will have a rising and fading phase. However, the blackbody temperature evolution is well described by the model, so we assume that on the time-scale considered here (100s of days for the IR echo), the outburst can be approximated by a short-lived pulse, where the inferred t_0 is the peak epoch of the pulse at luminosity $L_{\rm bol}$.

In Section 3.3.1, we established a peak luminosity of the IR echo of 2.3×10^{43} erg s^{-1}, and an energy budget of $\gtrsim 7.3 \times 10^{50}$ erg. A comparison with the peak outburst luminosity of $L_{\rm bol} \sim 0.1-1 \times 10^{45}$ erg s^{-1} implies a small dust covering factor ($L_{\rm IR}$ / $L_{\rm bol}$) of ∼1−10 per cent, which is consistent with the pre-outburst SED fit of the host, where the contribution to the IR emission by polar dust was small, see Fig. 10. Furthermore, the energy budget inferred from the IR echo constrains the grain radius a to $\gtrsim 0.1$ μm, as otherwise the luminosity would not be sufficient to fulfill the energy budget within the short time-scale (<100 d) of the pulse.

Finally, the inferred transient luminosity can be inserted back into equation (2) to solve for the sublimation radius where $T(R_{\rm sub}) = T_{\rm sub}$,

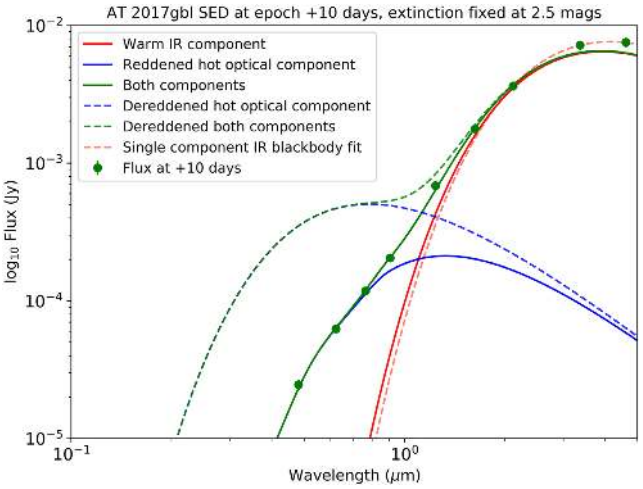

Figure 18. MCMC two components fit to all optical, near-IR and mid-IR fluxes of the epoch +10 d after discovery, with a fixed extinction at $A_{\rm V} = 2.5$ mag affecting the optical blackbody. In red is shown the warm IR component, in blue the dust-extincted optical component, and in green the sum of the blackbodies and the observed fluxes. The dashed lines indicate the de-reddened intrinsic optical blackbody in blue, and in red the single component fit of the IR blackbody.

and we obtain:

$$R_{\rm sub} = (1.8 \times 10^{17}\,{\rm cm}) \left(\frac{L_{\rm bol}/a_\mu}{10^{45}{\rm erg\,s^{-1}}} \right)^{1/2} \left(\frac{T_{\rm sub}}{1600\,{\rm K}} \right)^{5/2}, \quad (5)$$

which corresponds to a light crossing time of $R_{\rm sub}/c \simeq 70$ d.

3.3.4 *Two component fit of optical/IR epoch*

In addition to the bright IR detection of AT 2017gbl, the transient has also been detected at optical wavelengths. Fig. 18 shows the optical g, r, i, and z-band fluxes, as well as the IR fluxes, at the time of the first mid-IR epoch of 2017 July 18, +10 d after discovery, after correcting for Milky Way extinction. In i- and z-band the fluxes have been derived by interpolating the first two detections. With only a single g and r detection available, it was assumed that in the 8 d between the optical detection and the first mid-IR epoch, the transient had declined in flux in g- and r-band by the same fraction as in i-band. The figure also shows with the dashed red line the earlier derived blackbody fitted to the near-IR K_s-band and mid-IR fluxes, as shown in Fig. 16. It is clear that at shorter wavelengths there is flux in excess to the fitted warm blackbody.

At the longer wavelengths not only the first mid-IR epoch is well fitted with a warm blackbody, but so are all the subsequent epochs. Therefore, we assume that the optical excess at early times has a different origin, and explore whether the excess may be explained by a second blackbody peaking at shorter wavelengths, attenuated by some level of dust extinction. From the ratio of the broad emission lines, which we have connected to the transient event, we have inferred a line-of-sight extinction to the source of the broad line emission of ∼2.5 magnitudes in V (see Section 3.2.1). Therefore we fit the optical and IR fluxes of the first epoch simultaneously with two blackbody components, one warm component and one hot component, the latter of which we assume is dust-extincted by $A_{\rm V} = 2.5$ mag, where we adopt the Cardelli extinction law (Cardelli et al. 1989) with $R_{\rm V} = 3.1$. This assumption leaves four free parameters: the IR blackbody radius and temperature and the optical blackbody radius and temperature. We draw the IR priors from a Gaussian

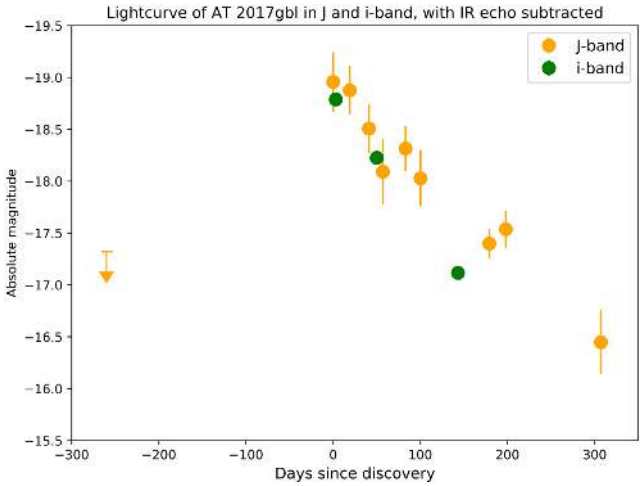

Figure 19. Evolution of AT 2017gbl in *i* and *J* after subtraction of the IR component, in absolute magnitudes. The magnitudes are dereddened for a line-of-sight extinction of $A_V = 2.5$ mag as determined through Paschen line ratios in Section 3.2.1, and corrected for the Milky Way extinction. Both filters show a similar continuous decline, from which we conclude the IR echo subtracted *J*-band flux traces the evolution time-scale of the optical blackbody component well. The *J*-band upper limit at epoch −260 d from 2016 October 21 is the latest pre-outburst epoch available to constrain the evolution of the optical component.

distribution centred on the earlier derived best estimates, with limits of 500–2500 K in temperature and 10^{-4} to 10^{-1} pc in radius. The optical blackbody radius and temperature are drawn from a flat prior ranging between 10^{-6} and 10^{-2} pc, and 3000 and 50 000 K, respectively.

Fig. 18 shows the resulting blackbody fit in log–log space. In red the warm IR component is shown, in blue the dust-extincted optical component and in green the sum of the blackbodies and the observed fluxes as green points. Also plotted is the de-reddened intrinsic optical blackbody. Fig. A1 shows the corresponding corner plot of the two-component fit, with well-behaved posterior distributions of all free parameters. The warm IR blackbody parameters from the two-component fit are very similar to the single component fitting results, with a radius of $3.24 \pm 0.1 \times 10^{-2}$ pc and a temperature of 1300 ± 12 K. The best estimates of the optical blackbody parameters are $0.081 \pm 0.011 \times 10^{-2}$ pc for the radius and 6500^{+1700}_{-1100} K for the temperature, with the uncertainties estimated by varying the line-of-sight extinction between +/− 1σ. The resulting optical blackbody luminosity is $0.8^{+0.7}_{-0.4} \times 10^{43}$ erg s^{-1}.

The remainder of the mid-IR epochs lack the optical photometry to accurately constrain a double component fit with four free parameters, as the transient declined rapidly in the optical. Only in the near-IR *J*-band is there a significant excess in flux over the warm IR blackbody, with the transient remaining visible for 307 d. In order to trace the evolution of the optical blackbody component, in Fig. 19 we plot the *i* and *J*-band absolute magnitudes after subtracting the IR blackbody flux inferred from the single component fits, and dereddening for a line-of-sight extinction of $A_V = 2.5$ mag and correcting for the Milky Way extinction. Here we assume the single component fits to the K_s and mid-IR fluxes describe the IR blackbody well, as was shown to be the case in the first epoch. As can be seen, both *i* and *J*-band show a similar continuous decline. As a result we conclude the *J*-band magnitude, with the IR echo contribution subtracted, traces the evolution time-scale of the optical blackbody well. This means the optical blackbody has faded below the detection limit at <370 d after the discovery. The epoch from −260 d before discovery constrains the rise of the optical blackbody, within the upper limit, while the peak epoch was estimated to be at -142 ± 11 d in Section 3.3.3.

3.4 Radio properties of AT 2017gbl

We detected radio emission from AT 2017gbl at both milli-arcsec (with the EVN and VLBA arrays) and arcsec scales (with VLA and AMI). Using the values from Table A7 we can obtain the spectral behaviour of AT 2017gbl at different epochs. At +38 d past discovery, we find a 4.4 to 7.6 GHz spectral index of 1.22 ± 0.16, which becomes less inverted by +99 d, with a value of 0.52 ± 0.14. Additionally, by +33 d the 15.5 GHz emission had started to decline and was already optically thin, while at 4.4 and 7.6 GHz it was still optically thick. This is shown by the less inverted spectral index in the same epoch between 4.4 and 15.5 GHz of 0.98 ± 0.12 and between 7.6 and 15.5 GHz of 0.79 ± 0.20. We estimate by eye the peak of the radio light curve between 13 and 15 d at 15.5 GHz, and between 150–200 d at 4.4/4.9 and 7.6 GHz. As seen in Fig. 7, the radio emission is transparent first at high frequencies (15.5 GHz) and later at lower frequencies. The detection of the mJy source at milliarcsec scales indicates a high brightness temperature. These characteristics correspond to a non-thermal, synchrotron origin of the radio emission.

The radio light curve of AT 2017gbl consists of only nine data points. We therefore tried to fit the radio light curve first considering only synchrotron self-absorption (SSA; see Weiler et al. 2002), and then considering pure free–free absorption (FFA). None of the fits reproduced the observed flux densities. The dust-obscured AGN potentially present in IRAS 23436+5257 could contribute to the compact emission observed with VLBI, which we have assumed is most likely dominated by AT 2017gbl in Table A7 and Fig. 7, see Section 2.5.1. The observed luminosity at 4.4/4.9 GHz is minimal at the EVN epoch of +587 d, which puts an upper limit on the quiescent AGN luminosity at 4.4/4.9 GHz of $<1.96 \pm 0.20 \times 10^{28}$ erg s^{-1} Hz^{-1}, or <40 per cent of the observed peak luminosity at 4.4/4.9 GHz. Given the time-scales of our observations, it is likely that AT 2017gbl is still contributing at the lower frequencies and the EVN epoch does not represent the quiescence level of the host. Additional VLBI observations over the next years will help establish if the compact radio source disappears completely and, if not, what the level of the quiescent AGN contribution is.

3.4.1 Implications of radio light curve

The radio emission comes from synchrotron emission by electrons accelerated by the shock driven by the outflow into the surrounding medium. The shock radius typically expands as a power-law function with time. For instance, in the Sedov–Taylor regime (appropriate after the shock has decelerated to non-relativistic speeds), the shock radius increases as $R \propto t^{2/(5-k)}$ and the shock speed decreases as $v \propto t^{-(3-k)/(5-k)}$ for a density profile $n(R) \propto R^{-k}$.

The radio spectrum evolution requires significant low-frequency absorption at early time due to either FFA or SSA. In either the FFA or SSA case, the characteristic absorption frequency at which the optical depth equals to unity evolves as a decreasing power-law function of time $\nu_a \propto t^{-p}$. Since the flux at a given frequency ν reaches the maximum when $\nu_a(t) \simeq \nu$, we can infer the peak times

(since outburst) at two different frequencies as follows:

$$\frac{\nu_1}{\nu_2} \sim \left(\frac{t_{\mathrm{peak},\nu_1}}{t_{\mathrm{peak},\nu_2}}\right)^{-p}. \quad (6)$$

For $\nu_1 = 15.5\,\mathrm{GHz}$ and $\nu_2 = 7.6\,\mathrm{GHz}$, we have $t_{\mathrm{peak},\nu_1} \simeq t_0 + 14\,\mathrm{d}$ and $t_{\mathrm{peak},\nu_2} \simeq t_0 + 175$ d (where t_0 is the pre-discovery explosion time), and hence $t_0 \simeq 150/(2^{1/p} - 1)$ d. This is in rough agreement with that inferred from the dust temperature evolution in Section 3.3.3, provided that $p \sim 1$ (for $p \in (0.5, 1.5)$, we have $t_0 \simeq 50$ to $250\,\mathrm{d}$). In the following, we discuss the two absorption scenarios for which we calculate the power-law index p.

In the FFA case, the optical depth is given by $\tau_{\mathrm{ff}}(\nu) \simeq 3.4 \times 10^{-28} T_4^{-1.3} \nu_{15.5\,\mathrm{GHz}}^{-2.1}$ EM, where $\mathrm{EM} = \int n^2 \mathrm{d}\ell \sim n^2 R$ is the emission measure (Draine 2011) in units of cm^{-5}. For electron temperature $T \gtrsim 10^4$ K and shock radius $R \lesssim 200$ light days, we obtain a lower limit on the density of the surrounding medium $n \gtrsim 10^5\,\mathrm{cm}^{-3}$. It is possible to estimate EM by the luminosity of Paschen α recombination line, by assuming a uniform HII cloud whose size is given by the linewidth according to Keplerian motion. The resulting EM is indeed much greater than $10^{28}\,\mathrm{cm}^{-5}$, meaning that the low-frequency radio emission is likely free–free absorbed if the shock is buried below the H II cloud. However, the estimate is subjected to uncertainties of clumpiness and electron temperature. More generally, for a power-law density profile $n(R) \propto R^{-k}$, we have $\mathrm{EM} \propto R^{1-2k} \propto t^{2(1-2k)/(5-k)}$, so we obtain $\nu_\mathrm{a} \propto t^{(1-2k)/(5-k)}$. Thus, we have $p \in (0.5, 1.5)$ for density profile $k \in (1.4, 2.4)$.

In the SSA case (Chevalier 1998), the specific luminosity near the self-absorption frequency ν_a is given by $L_{\nu_\mathrm{a}} \simeq 4\pi^2 R^2 (2\nu_\mathrm{a}^2/c^2) \gamma_\mathrm{a} m_\mathrm{e} c^2$, where γ_a is the Lorentz factor corresponding to a characteristic synchrotron frequency of ν_a. For shock speed $v = \beta c$ and pre-shock medium density n, the magnetic field strength in the shocked region is given by $B \simeq \sqrt{16\pi\epsilon_\mathrm{B} n m_\mathrm{p} v^2} = (0.87\,\mathrm{G})\,\epsilon_{\mathrm{B},-1}^{1/2} n_4^{1/2} \beta_{-1}$, where ϵ_B is the fraction of energy in B-fields. Then, the Lorentz factor is given by $\gamma_\mathrm{a} \simeq 80\,\nu_{\mathrm{a},15.5\,\mathrm{GHz}}^{1/2} \epsilon_{\mathrm{B},-1}^{-1/4} n_4^{-1/4} \beta_{-1}^{-1/2}$. Thus, the shock radius is well constrained by the observed L_{ν_a} and ν_a,

$$R \simeq (8.7 \times 10^{15}\,\mathrm{cm})\, L_{\nu_\mathrm{a},29}^{1/2} \nu_{\mathrm{a},15.5}^{-5/4} \epsilon_{\mathrm{B},-1}^{1/8} \left(n_4 \beta_{-1}^2\right)^{1/8}. \quad (7)$$

Ignoring the weak dependencies on ϵ_B, density n and shock speed β, we obtain $R \propto L_{\nu_\mathrm{a}}^{1/2} \nu_\mathrm{a}^{-5/4} \propto t^{2/(5-k)}$. We plug in $\nu_1 = 15.5\,\mathrm{GHz}$, $L_{\mathrm{peak},\nu_1} = 10^{29}\,\mathrm{erg\,s^{-1}\,Hz^{-1}}$, $\nu_2 = 7.6\,\mathrm{GHz}$, and $L_{\mathrm{peak},\nu_2} = 8 \times 10^{28}\,\mathrm{erg\,s^{-1}\,Hz^{-1}}$, and then obtain $(t_{\mathrm{peak},\nu_1}/t_{\mathrm{peak},\nu_2})^{2/(5-k)} \simeq 0.5 \simeq \nu_2/\nu_1$, and hence $p \simeq 2/(5-k)$. Thus, the power-law index in equation (6) is $p \in (0.5, 1.5)$ for density profile $k \in (1, 3.7)$.

Another potentially useful quantity that can be derived from the radio data is the total energy of the outflow. Regardless of the absorption scenario, the number of electrons radiating at frequency $\nu = 15.5\,\mathrm{GHz}$ near the flux peak (when the system is marginally optically thin) can be estimated by $N_\mathrm{e} = L_\nu/P_\nu$, where $P_\nu \simeq e^3 B/m_\mathrm{e} c^2$ is the synchrotron specific power. One way of estimating the minimum energy of the outflow is $E_\mathrm{min}^{(1)} \sim \epsilon_\mathrm{e}^{-1} N_\mathrm{e} \gamma m_\mathrm{e} c^2$, where $\epsilon_\mathrm{e} \sim 0.1$ is the fraction of energy in electrons. Thus, we obtain

$$E_\mathrm{min}^{(1)} \sim (5 \times 10^{47}\,\mathrm{erg})\, \epsilon_{\mathrm{B},-1}^{-3/4} \left(n_4 \beta_{-1}^2\right)^{-3/4}. \quad (8)$$

Our fiducial value for ϵ_B is conservative, because it is usually inferred to be much less than 0.1 (in that case, the total energy is much larger). Another way of estimating the outflow energy is to add up the total energy of protons behind the shock $E_\mathrm{min}^{(2)} \sim (4\pi/3) R^3 n \beta^2 m_\mathrm{p} c^2/2 \simeq (3 \times 10^{47}\,\mathrm{erg})\, R_{16}^3 n_4 \beta_{-1}^2$. From equation (7), we know that $R \gtrsim 10^{16}\,\mathrm{cm}$, because otherwise the emission at 15.5 GHz will be self-absorbed. Increasing the product $n\beta^2$ will decrease $E_\mathrm{min}^{(1)}$ but increase $E_\mathrm{min}^{(2)}$. Overall, we constrain the total energy of the outflow to be more than 3×10^{47} erg.

Additionally, we provide a lower limit for the total number of electrons in the shocked region[11] $N_\mathrm{tot} \gtrsim N_\mathrm{e}\gamma$. And then, in the SSA scenario, the density of the surrounding medium is constrained to be $n \sim N_\mathrm{tot}/R^3 \gtrsim 10^4\,\mathrm{cm}^{-3} \epsilon_{\mathrm{B},-1}^{-0.5} \beta_{-1}^{-1}$. Since we also obtain $n \gtrsim 10^5\,\mathrm{cm}^{-3}$ in the FFA scenario, we conclude that the circumnuclear medium of AT 2017gbl is unusually dense, which may be the physical reason why the source is radio bright.

3.5 X-ray properties of AT 2017gbl

The luminosity of the X-ray source observed at the position of AT 2017gbl at +118 d was $L_{0.5\text{–}8\mathrm{keV}} = 3.2 \times 10^{41}\,\mathrm{erg\,s^{-1}}$. In addition to a potential contribution by the transient, several emission components of the host galaxy (X-ray binaries, hot gas, and AGN) can also contribute to the observed luminosity. Lacking a quiescent X-ray epoch, we estimate the host galaxy contribution using an empirical relationship between the X-ray luminosity of a LIRG and its star formation rate: $L_{0.5\text{–}8\,\mathrm{keV}} \approx 3.7 \times 10^{39\pm0.4} \frac{\mathrm{SFR}}{(\mathrm{M_\odot\,yr^{-1}})}\,\mathrm{erg\,s^{-1}}$ (e.g. Mineo et al. 2012; using the scaling factor for unresolved galaxies). Here the X-ray emission originates primarily from the galaxy's population of X-ray binaries and is expected to remain constant on the time-scales we consider. Following Mineo et al. (2012) we estimated the SFR following their equations (9) and (10), assuming a negligible fraction of the IR luminosity being due to the old stellar population and a negligible amount of SFR observable in the near-UV. In this way we obtain an SFR of $69\,\mathrm{M_\odot\,yr^{-1}}$ using exactly the same approach as Mineo et al. (2012) in their analysis. This corresponds to $L_\mathrm{X} \sim 3 \times 10^{41}\,\mathrm{erg\,s^{-1}}$. Therefore, the observed X-ray emission may be entirely explained by the host galaxy.

4 DISCUSSION

In this section, we discuss the nature of AT 2017gbl implied by various key observations. We consider the scenarios of an SN, a CLAGN, and a TDE. We aim to explain the following:

(i) The IR SED of AT 2017gbl is consistent with a single component blackbody throughout its evolution, indicating dust emitting at a narrow range of temperatures and a negligible amount of foreground extinction to the IR emitting region. Its integrated radiation emitted from +10 to +855 d after discovery is 7.3×10^{50} erg. This value is a lower limit to the total radiated energy of the underlying transient, as AT 2017gbl was discovered at, or post, the IR peak brightness, and at mid-IR wavelengths has not fully faded yet.

(ii) The GNIRS spectrum obtained at +55 d past discovery shows prominent, broad Paschen, Brackett, He I and O I emission features with FWHM $\sim 2000\,\mathrm{km\,s^{-1}}$, which have diminished or disappeared in the GNIRS spectrum at +503 d. The pre-outburst near-IR K-band OSIRIS spectrum does not show signs of broad emission features in the Brackett lines. Similarly, the optical ISIS spectrum obtained at +2 d past discovery shows a prominent broad H α feature, which diminished over time.

(iii) The discovery epoch shows flux at optical wavelengths that is not explained by the IR echo. Assuming the optical emission is affected by a dust extinction of $A_\mathrm{V} = 2.5$ mag, inferred from the line ratio of the broad Paschen emission lines, it is well fitted with a blackbody of ~6500 K.

[11] The number of electrons with Lorentz factor order unity is at least a factor of γ larger than that of the emitting electrons N_e (near Lorentz factor γ).

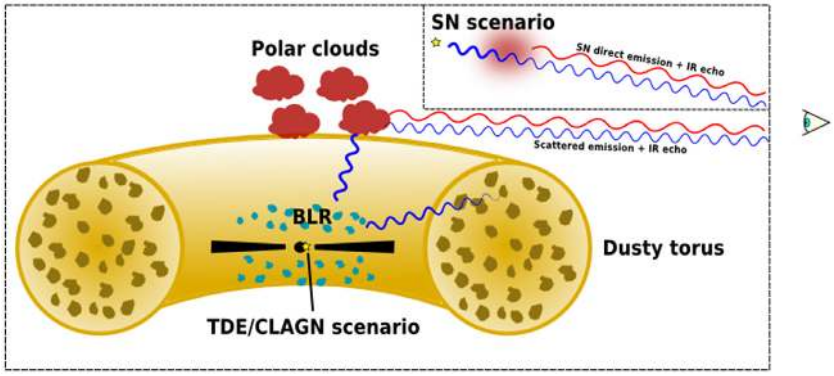

Figure 20. A schematic diagram showing the sources of IR and optical emission (and absorption) in the scenarios for AT 2017gbl either as an SN, or a TDE/CLAGN. Note the components are not to scale. In all scenarios the IR emission is interpreted as an IR echo, where UV/optical emission from the transient is absorbed and re-radiated at IR wavelengths. The optical emission in the case of an SN is considered direct dust-attenuated emission, whereas in the case of a TDE/CLAGN it is considered scattered light originating in the BLR. Direct emission from a TDE/CLAGN is not visible due to the presence of the dusty torus along the line of sight. It must be noted that the potential SN location is not constrained, however, there is 2.5 mag of extinction along the line of sight.

(iv) The radio emission is of synchrotron origin, peaking around 13–15 d past discovery at 15.5 GHz with observed host-subtracted peak luminosity of 8.4×10^{28} erg s^{-1} Hz^{-1}, and 150–200 d past discovery at 4.4/4.9 GHz with an observed peak luminosity of 5.2×10^{28} erg s^{-1} Hz^{-1}.

(v) The rise time to the peak IR luminosity is constrained to $\lesssim$140 d, as inferred from the IR blackbody temperature evolution. The subsequent decline of the IR echo is traced by the mid-IR observations, where the transient has faded close to the detection limit at +855 d. The evolution of the optical component is loosely constrained by the IR echo subtracted *J*-band light curve with a rise time of <260 d and decline to the detection limit within <370 d.

To aid the discussion, Fig. 20 shows a schematic of the geometry and origin of the different emission and absorption components in the three different scenarios discussed here.

4.1 Supernova

SN types other than Type II are ruled out, as the IR spectra show prominent broad hydrogen lines, such as Paschen α and β, which we have associated with the transient through its evolution. Based on the energy budget of AT 2017gbl inferred from its integrated IR luminosity, normal Type II SNe are also excluded as a viable scenario, as they typically have a total bolometric radiated energy output of less then 10^{49} erg (Utrobin 2007).

Notable exceptions are the most luminous and long-lasting Type IIn SNe such as SN 2010jl (Andrews et al. 2011; Fox et al. 2013; Fransson et al. 2014), SN 2015da (Tartaglia et al. 2020), and SN 1988Z (Aretxaga et al. 1999), which have been observed to emit $>10^{50}$ erg and display prominent hydrogen emission lines from the interaction of the SN ejecta with H-rich circumstellar gas. Furthermore, many Type IIn SNe have been observed to show prominent long-lasting mid-IR emission, most likely due to re-radiation by pre-existing dust (Fox et al. 2011).

The coverage of SN 2010jl and SN 2015da spanned several years, and extended from the optical to the mid-IR, which allows for a detailed comparison with AT 2017gbl. The SEDs of SN 2010jl (Fransson et al. 2014) and SN 2015da (Tartaglia et al. 2020) were shown to be well represented by a combination of a hot blackbody peaking in the optical and a warm blackbody peaking in the IR, with the IR components lagging the optical components in luminosity by

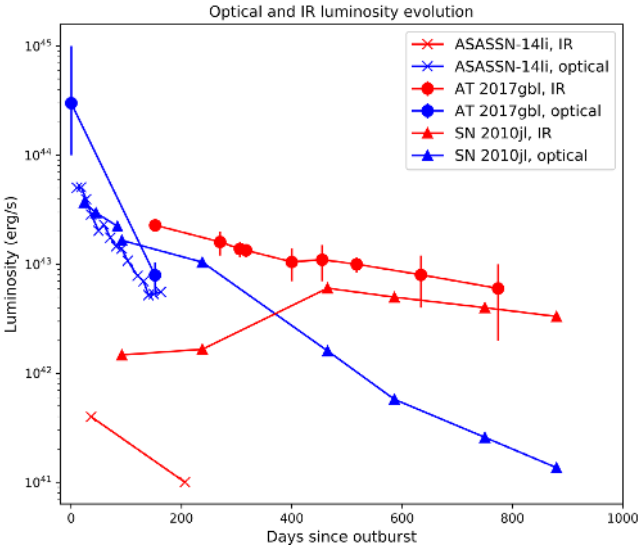

Figure 21. Evolution of the blackbody luminosities of the optical and IR components of AT 2017gbl, SN 2010jl (Zhang et al. 2012; Fransson et al. 2014), and ASASSN-14li (Holoien et al. 2016; Jiang et al. 2016). The first three optical epochs of SN 2010jl are based on bolometric luminosities from Zhang et al. (2012), which should be close to its optical blackbody luminosity because the IR component was negligible at early times. The x-axis start at the outburst epoch (−142 d) of AT 2017gbl inferred in Section 3.3.3, the explosion epoch (MJD 55478) of SN 2010jl (Fransson et al. 2014), and the discovery epoch (MJD 56983) of ASASSN-14li (Holoien et al. 2016). The optical luminosity of AT 2017gbl at day 0 is the range inferred from fitting the blackbody temperature evolution in Section 3.3.3.

400–600 d, see Fig. 21 for the IR and optical blackbody luminosity light curves of SN 2010jl. For both SN 2010jl and SN 2015da, the optical component was considered direct photospheric emission from the SN and emission originating in the interaction between the ejecta and the circumstellar gas, and the IR component interpreted as an IR echo. We assume a similar scenario for AT 2017gbl, see Fig. 20, where the optical emission from AT 2017gbl is direct SN emission, affected by a line-of-sight extinction of $A_V = 2.5$ mag inferred from the Paschen line ratio.

4.1.1 Energetics

As shown in Fig. 21, the optical blackbody luminosity of SN 2010jl peaked around discovery at $\sim 4 \times 10^{43}$ erg s^{-1} (similar to SN 2015da), and in the first 100 d declined by ∼50 per cent. The total radiated energy of SN 2010jl, excluding the IR echo, was estimated to be 6.5×10^{50} erg, very similar to SN 2015da at 6.3×10^{50} erg. This already makes SNe 2010jl and 2015da among the most energetic Type IIn SNe observed to date. In both cases the very large energetics were explained by the efficient conversion of the kinetic energy into radiation requiring extremely large mass-loss rates of ∼0.1 and 0.6 $M_\odot$ yr^{-1}, respectively (Fransson et al. 2014; Tartaglia et al. 2020). In comparison, the optical luminosity of AT 2017gbl at the peak, inferred from the IR blackbody temperature evolution in Section 3.3.3, was 10^{44}–10^{45} erg s^{-1}. According to our observations it declined by at least an order of magnitude down to $0.8^{+0.7}_{-0.4} \times 10^{43}$ erg s^{-1} at +10 d after the discovery (or +152 d after the peak epoch inferred in Section 3.3.3). This results in a total radiated energy for AT 2017gbl, excluding the IR echo, of 7×10^{50} to 7×10^{51} erg over the first 150d since the peak, which corresponds to ∼1 to 10 times the energy budget of SN 2010jl and SN 2015da in the optical.

The energetics of the IR echo of AT 2017gbl are better constrained, and clearly exceed those of SN 2010jl and SN 2015da. The IR components of SN 2010jl and SN 2015da peaked at luminosities well below that observed for AT 2017gbl, by factors of at least ∼4 and 15, respectively, see Fig. 21. As a consequence, the total energy emitted by their IR echoes was significantly less than observed in the case of AT 2017gbl, at 2.7×10^{50} erg for SN 2010jl and 8.5×10^{49} erg for SN 2015da (up to day 1233). The energy radiated by the IR echo of AT 2017gbl is 7.3×10^{50} erg, which as discussed in Section 3.3.1 is considered a lower limit.

The total radiated energies of the IR echoes of SNe 2010jl and 2015da amount to ∼40 per cent and ∼10 per cent, respectively, of their optical components. Here it is noteworthy that SN 2010jl is one of the most luminous Type IIn SNe observed to date, and brighter at 4.5 μm than the brightest mid-IR detections of the Fox et al. (2011) sample of Type IIn SNe. Assuming that most of the energy of AT 2017gbl in the optical was radiated in the first 150 d given its rapid *J*-band decline, the energy radiated by its IR echo lies between 10 and 100 per cent of the energy radiated in the optical. If this fraction was similar to that of SN 2010jl and SN 2015da, the total energy associated with AT 2017gbl would be substantially greater than the total energies of SNe 2010jl and 2015da.

4.1.2 IR emission lines

The emission lines that we can unambiguously associate with AT 2017gbl based on their evolution are Paschen α–β, He I λ10830, O I λλ8445, and 11290, all with a width of ∼2000 km s^{-1}, see Table 2. Both SN 2010jl and SN 2015da show the same emission lines, but they are narrower. The Paschen lines of SN 2015da evolve from ∼600 km s^{-1} at epoch +26 d to 1100–1300 km s^{-1} at epoch +607 d. Intermediate width lines of a few 1000 km s^{-1} are seen in 1988Z-like SNe such as 2005ip and 2006jd (Stritzinger et al. 2012), but they are accompanied by much stronger H emission lines with FWHM of $\sim 10^4$ km s^{-1} for the first few hundred days, which we would likely see in our spectra.

4.1.3 Radio luminosity and time-scale

The radio peak luminosity and the time to peak of AT 2017gbl agree well with those observed for the radio emitting SNe of Type IIn and, marginally also, for SNe of Type Ibc, whose time to peak is usually well below 100 d (Perez-Torres et al. 2015). However, in the radio, SN 2010jl was fainter than other Type IIn SNe and was only detected with the VLA after ∼500 d from the explosion. The 5 GHz emission was estimated to have peaked around 900 d from the explosion, implying that FFA was likely the dominant process resulting in the slow rise to the maximum (Chandra et al. 2015). Similarly, in the case of the extremely luminous and long-lasting Type IIn SN 1988Z that was observed to radiate 2×10^{51} erg (Aretxaga et al. 1999) the radioemission was observed to peak at 5 GHz at an epoch of ∼900 d as a result of FFA arising in the dense circumstellar medium (CSM) (Williams et al. 2002).

It is clear that the radio evolution of AT 2017gbl differs significantly from that of SNe 2010jl and 1988Z. First, the light curve was not fitted well by SSA or FFA models, see Section 3.4. A possible explanation is that the transient is not well explained by spherically expanding material, as expected in the case of, e.g. an SN. Secondly, assuming an outburst epoch of −142 d before discovery, at 15.5 GHz the radio light curve was observed to peak very early, around ∼150 d, with a peak luminosity of $\sim 1 \times 10^{29}$ erg s^{-1} Hz^{-1}. At 4.4/4.9 GHz our VLBI observations indicate the transient peaked and became optically thin some time around ∼300–350 d. Following Pérez-Torres et al. (2009a) we find that if AT 2017gbl was a Type II SN, then it would have a mass-loss rate of the order of 5×10^{-5} $M_\odot$ yr^{-1}, assuming a wind velocity of 10 km s^{-1}. Such a mass-loss rate is more typical of less massive progenitors that, on the other hand, should not have yielded such an energetic event as observed in the IR. Therefore, the radio properties of AT 2017gbl are not consistent with those observed for the most luminous and slowly declining Type IIn SNe that are powered by interaction with a massive and dense CSM resulting from extremely high mass-loss rates.

We note that also Type II superluminous SNe (SLSN) have been observed to radiate up to 5×10^{51} erg of energy (Nicholl et al. 2020), and display prominent hydrogen emission in their spectra (e.g. Inserra et al. 2018). The Type II class is dominated by the so-called Type IIn SLSNe (Gal-Yam 2019), which technically includes SN 2010jl. Other types of Type II SLSNe are rare, and as such we deem our analysis of Type IIn SNe as a scenario for AT 2017gbl to be also applicable for Type II SLSNe.

In summary, based on the combination of both the energetics inferred from our IR observations, as well as the luminosity and evolution time-scale of the radio counterpart, we do not deem an SN scenario a plausible explanation for AT 2017gbl.

4.2 Changing look AGN

Since AT 2017gbl is coincident at the AO resolution with the Northern nucleus of IRAS 23436+5257, which potentially hosts a dust-obscured AGN, it is natural to consider their relation. As argued in Section 3.1.1, the observed variability in the IR is difficult to reconcile with what would be considered as normal AGN variability. However, mid-IR variability with similar amplitude and luminosities as AT 2017gbl have been observed in CLAGN (Sheng et al. 2017, 2020; Stern et al. 2018), where it was interpreted as hot-dust emission echoing drastic drops or rises in accretion rate of the central AGN. If AT 2017gbl is related to a dramatic change in the accretion rate by the central SMBH, no direct line of sight is available to the transient event at optical and IR wavelengths due to the obscuration of ∼300 mag in A_V through the dusty torus, see Section 3.1.

4.2.1 Geometry of the system

In the CLAGN scenario, we interpret the IR echo to have originated in dust clouds along the polar axis to which we have a direct line of sight, a geometry which has been observed in dust-obscured AGN (Asmus 2019). The broad spectral lines associated with AT 2017gbl in the near-IR (Paschen α–δ, He I λ10830, and O I $\lambda\lambda$8445, and 11290) are common to the BLR of AGN (e.g. Landt et al. 2008). This leads us to conclude the broad spectral features, as well as the optical emission, originate in the BLR, the flux of which responds to an increase from continuum photons from the AGN, lagged by some period due to light traveltime delays (Peterson et al. 2004). However, the BLR is fully obscured by the dusty torus, so the observed BLR emission would have to have been scattered into our line of sight, after being initially emitted in the polar direction, unobscured by the dusty torus. Such a geometry has also been observed in, e.g. NGC 1068, a Seyfert 2 galaxy in which polarization spectra of the nucleus exhibited broad Balmer lines indicative of a Type 1 AGN hidden behind the torus (Antonucci & Miller 1985; Marin 2018). The origin of the scattered light in this case would be clouds along the polar axis, where we also expect the IR echo to have originated from. The dust extinction of $A_V = 2.5$ mag inferred from the Paschen line ratios is then interpreted as the combined extinction along the line of sight from the AGN BLR via the scattering regions to the observer. This geometry is visualized in Fig. 20.

4.2.2 Time-scales in the optical and IR

CLAGN are typically identified by comparing archival spectra from years ago with recent data (e.g. MacLeod et al. 2016). Only in recent years, due to widefield synoptic surveys, has imaging data become available to construct (sparsely sampled) light curves of the outbursts related to CLAGN. The observed optical time-scales involved are typically of order of 1000s of days (Yang et al. 2018; MacLeod et al. 2019; Graham et al. 2020). Based on the IR echo subtracted *J*-band light curve of AT 2017gbl (see Fig. 19), which acts as a tracer of its optical blackbody, the time-scale (incl. rise and decline) of the optical variability of AT 2017gbl is limited to <630 d. This time-scale is very short for a CLAGN, although there have been recent discoveries of unusual fast evolving CLAGN (Frederick et al. 2019; Trakhtenbrot et al. 2019).

Similarly, the IR echoes associated with CLAGN have typical time-scales that are much slower than observed for AT 2017gbl. The time-scale of mid-IR variability observed by Sheng et al. (2017) in a sample of 10 known CLAGN ranged between 3.5 and 4.5 yr, both in fading and brightening. Similar mid-IR fading time-scales of 4–6 yr were observed by Sheng et al. (2020) for a sample of six quasars, spectroscopically classified as 'turn-off' CLAGN. The fastest evolving IR echo associated with a CLAGN is a bright mid-IR flare in SDSS1115+0544 discovered by Yan et al. (2019), which they interpreted to result from a 'turn-on' AGN rather than a TDE or Type IIn SN, based on the light-curve evolution and a UV detection at late times. Its *WISE* mid-IR lightcurve peaked ∼1 and ∼1.5 yr after the last pre-outburst epoch in *W*1 and *W*2, respectively, at luminosities similar to AT 2017gbl. Inspection of the NEOWISE-R archive shows the transient in SDSS1115+0544 is still steadily declining in the mid-IR, four years after the peak.

These time-scales are in contrast with the rise time of the IR echo of AT 2017gbl, which is limited to $\lesssim$140 d. The *Spitzer* mid-IR light curve of the host nucleus of AT 2017gbl has declined close to the pre-outburst levels at +855 d (2.3 yr) after the discovery. This time-scale would suggest AT 2017gbl also evolved faster in its mid-IR decline compared to the sample of CLAGN, although the contrast is less distinct than for the rise.

Recently, Cannizzaro et al. (2020) laid out a detailed analysis of the time-scales involved with AGN accretion rate changes, in order to explain the time-scales involved with nuclear transient Gaia16aax, which rose to peak in the optical in ∼200 d. They concluded that most of the proposed accretion disc variability mechanisms are on time-scales longer than observed for Gaia16aax, and/or not resulting in a sufficiently large amplitude. As with SDSS1115+0544, the observed rise to the peak with *WISE* in the mid-IR of Gaia16aax at ∼1 yr was significantly slower than the observed optical rise to the peak. The light curve of an IR echo lags the optical light curve due to light traveltime effects, and will thus show slower evolution, which depends on the dust geometry (e.g. Lu et al. 2016). The IR echo of AT 2017gbl rose to the peak in $\lesssim$140 d, which implies an even faster evolution in the optical.

The only CLAGN for which radio variability is reported in the literature is Mrk 590 (Koay et al. 2016), a Seyfert galaxy which has been declining in accretion rate over the past decade (Denney et al. 2014). The CLAGN was observed to increase in flux at 1.4 GHz by 28 per cent over 12 yr, followed by a decrease in flux of 48 per cent over the following 20 yr. These amplitudes and time-scales are again in stark contrast with AT 2017gbl, which at 4.4 GHz doubled in flux in 63 d, followed by a drop of >60 per cent in the following 488 d.

In summary, if AT 2017gbl is a result of a dramatic change in accretion by the dust-obscured AGN, the time-scale of these changes is limited by the observed time-scales of the mid-IR, optical, and radio light curves. The pre-outburst *J*-band limit and subsequent decline of the optical emission constrains the period of optical variability to <630 d, including the pre-outburst limit of −260 d. The observed rise to the peak of the IR echo in $\lesssim$140 d implies the optical rise was much faster, further constraining the period of intensified accretion which ionized the BLR. Similarly, the radio evolution of AT 2017gbl showed variability of amplitudes and time-scales which have not been observed for CLAGN. In conclusion, if AT 2017gbl is due to a CLAGN, it would be one of the fastest evolving CLAGN, with a unique radio light curve.

4.3 Tidal disruption event

TDEs have been observed to radiate up to 10^{51}–10^{52} erg (e.g. Holoien et al. 2016; Mattila et al. 2018) with peak luminosities up to $\sim 10^{45}$ erg s^{-1} (e.g. van Velzen et al. 2020), which satisfies the energy budget and the inferred peak luminosity of AT 2017gbl. Furthermore, TDEs evolve in the optical over time-scales of 200–250 d (e.g. van Velzen et al. 2020), within the limits imposed by the time-scale of the optical emission of AT 2017gbl. Assuming the presence of an AGN the interpretation of the IR emission as an IR echo and the optical component of AT 2017gbl being dominated by the BLR emission scattered into our line of sight by polar clouds is the same as in the CLAGN scenario (see Fig. 20).

The optical blackbody temperature of 6500 K derived in Section 3.3.4 from the early optical emission of AT 2017gbl is not consistent with direct emission of optical/UV selected TDE candidates, since their early-time emission is characterize by blackbody temperatures of around 2×10^4 K (e.g. Hung et al. 2017). However, recent simulations of TDEs occurring in AGN have shown that the spectrum of the resulting transient may not look like a standard TDE and it is even uncertain in which energies the radiation emerges from the event (Chan et al. 2019). Furthermore, substantial reprocessing of the TDE emission may have occurred within the dense BLR clouds. In Fig. 21 we show the optical luminosity

evolution of the prototypical TDE ASASSN-14li (Holoien et al. 2016). Within uncertainties, the optical peak luminosity and decline rate of AT 2017gbl is similar to that of ASASSN-14li. Notably, ASASSN-14li occurred in a galaxy where the presence of an AGN is suspected based on radio observations (van Velzen et al. 2016a; Bright et al. 2018).

4.3.1 IR echoes

The presence of IR echoes in TDEs has been established only during the past few years. Lu et al. (2016) showed through model calculations that depending on the total radiated energy in the UV-optical and the sky covering factor of the dust clouds the dust emission following a TDE peaks at 3–10 μm with typical luminosity between 10^{42} and 10^{43} erg s^{-1}. By now such IR echoes have been observed for several TDEs. For example, Jiang et al. (2016) discovered a significant mid-IR increase in the *WISE* data of ASASSN-14li 36 d after the discovery. By fitting the quasi-simultaneous broad-band SED with a two-component blackbody, they determined an integrated IR luminosity of 2.5×10^{41} erg s^{-1}, see Fig. 21. Similarly, Dou et al. (2016) estimated mid-IR luminosities in the range of 0.4–2.0 $\times 10^{43}$ erg s^{-1} for four TDE candidates, and van Velzen et al. (2016b) reported on 3.4 μm emission of $\sim 10^{42}$ erg s^{-1} for three previously known TDE candidates.

The observed IR echoes arising from the TDE candidates span a wide range both in terms of IR luminosity, from 10^{41} erg s^{-1} for ASASSN-14li to 10^{44} erg s^{-1} in the case of the flare in IRAS F01004-2237 (Dou et al. 2017); as well as in duration, from ∼500 d for TDEs discussed in van Velzen et al. (2016b) to > 4000 d for Arp 299-B AT1 (Mattila et al. 2018). In comparison, the IR echo of AT 2017gbl was relatively bright with a peak IR luminosity of $\sim 2.3 \times 10^{43}$ erg s^{-1}. In terms of time-scale, the evolution of the IR echo of AT 2017gbl was comparable to those TDEs with fast-paced IR echoes, such as PTF-09ge and PTF-09axc (van Velzen et al. 2016b) and ASASSN-14li (Jiang et al. 2016). The IR echo of AT 2017gbl rose to peak in $\lesssim$140 d, and was only marginally detected in the mid-IR in the last epoch of +855 d, having already faded in the near-IR after 590 d. We note that the time-scales of IR emission likely reflect the geometry of the dust responsible for the re-radiation of the UV/optical emission (through light traveltime effects) rather than the actual time-scales of that emission (e.g. Lu et al. 2016). PTF-09ge and PTF-09axc were detected at or after peak in the mid-IR some 200 d after the optical peak of the TDE, and the IR echo of ASASSN-14li peaked only 36 d after the optical TDE discovery. All three faded in the mid-IR in <500 d.

Based on our IR observations, the total radiated energy of AT 2017gbl was at least 7.3×10^{50} erg. Following Metzger & Stone (2016) and assuming 10 per cent as the accreted fraction and 10 per cent as the radiative efficiency we find that a star with a mass above 0.1 $M_\odot$ can explain the energetics of AT 2017gbl. Stars with such a mass can be disrupted by a non-spinning BH at the lower end of the mass range of $\log_{10}(M_{BH}) = 7.1 \pm 0.4\,M_\odot$ estimated for the SMBH at the centre of IRAS 23436+5257 (Law-Smith et al. 2017). Outflows, which are responsible for the radio emission, can be generated by the self-crossing of the fallback stream (Lu & Bonnerot 2020) or the accretion disc wind (Strubbe & Quataert 2009).

4.3.2 TDEs in LIRGs

Although TDEs are still a relatively rare phenomenon with observed rates of $\sim 10^{-8}$ yr^{-1} Mpc^{-3} (e.g. van Velzen 2018), there have now also been two TDE (candidates) discovered in (U)LIRGs, both showing long-lasting IR emission. Tadhunter et al. (2017) reported the discovery of a bright nuclear transient in the ULIRG IRAS F01004-2237. They interpret the transient as a TDE based on strong and variable broad He I λ5876 and He II λ4686 lines in their spectrum. More recently, however, Trakhtenbrot et al. (2019) favoured an origin of intensified accretion into the SMBH. The optical transient in IRAS F01004-2237 was followed by an IR echo spanning several years with a peak mid-IR luminosity of 2–3 $\times 10^{44}$ erg s^{-1} (Dou et al. 2017).

Mattila et al. (2018) reported the discovery and follow-up of an extremely energetic transient Arp 299-B AT1 in the LIRG Arp 299, with the IR luminosity peaking at $\sim 6 \times 10^{43}$ erg s^{-1}. Over a decade of VLBI observations a resolved and expanding off-axis radio jet was detected coincident with the position of Arp 299-B AT1, showing that the transient had arisen from a TDE. The IR emission was interpreted to originate from dust, in the polar regions of the AGN torus viewed almost edge-on, responsible for absorbing and re-radiating much of UV-optical emission of the transient.

Similar to AT 2017gbl, Arp 299-B AT1 was observed in the near- and mid-IR and its IR SED was well described by an expanding and cooling blackbody. In both cases the IR SED was well described by a single component blackbody indicating a narrow range of temperatures and only a small amount (in the IR) of extinction in the foreground to the IR emitting region. In the first ∼560 d its IR blackbody parameters evolved from $(4.23 \pm 0.06) \times 10^{-2}$ pc to $(8.83 \pm 0.09) \times 10^{-2}$ pc, and from 1045 ± 7 to 902 ± 5 K, in radius and temperature, respectively. These values are remarkably similar to those of AT 2017gbl, see Table 4. However, in the case of AT 2017gbl the blackbody temperature declined much more rapidly resulting in a decreasing luminosity, while Arp 299-B AT1 increased in IR luminosity for over 2000 d. Consequently, the energy budget of Arp 299-B AT1 inferred from its IR emission is much larger at $>1.5 \times 10^{52}$ erg. Initially, no optical counterpart was observed for Arp 299-B AT1 and only deep archival *HST* observations allowed a possible optical counterpart to be identified through image subtraction. The optical depth through the dusty torus towards the central engine in Arp 299-B1 is extremely large, corresponding to an optical extinction of $\sim 10^3$ mag. Therefore, the optical emission (if related to Arp 299-B AT1) can only be explained as scattered light from the gas and dust in the polar regions. The differences in the IR and optical properties between Arp 299-B AT1 and AT 2017gbl could arise from differences in the geometry and extent of the dusty regions surrounding the UV-optical transient, as well as the properties of the SMBH and the disrupted star.

4.3.3 Radio

The peak radio luminosity of AT 2017gbl is three to four times higher than the peak luminosities of the TDEs ASASSN-14li and Arp 299-B AT1. However, the radio evolution of AT 2017gbl appears to be more similar to that of ASASSN-14li, whose 5.0 GHz emission peaked at about 150 d, and at ∼50 d at 15.7 GHz (Bright et al. 2018). On the contrary, the radio emission from Arp 299-B AT1 peaked much later, close to ∼1000 d after the event. The nature of the radio emission in ASASSN-14li is still under debate, and is unclear whether it was powered by a jet or by an expanding, non-relativistic outflow (e.g. Alexander et al. 2016; van Velzen et al. 2016a; De Colle & Lu 2019). The nature of the radio emission in Arp 299-B AT1 is clear: a relativistic jet that decelerated due to its huge surrounding density (Mattila et al. 2018). The bright radio emission in these events is likely due to high densities in the surrounding medium. Our VLBI observations could not resolve the radio morphology of AT 2017gbl,

and therefore we cannot at this stage confirm, or rule out, whether the radio emission of AT 2017gbl is powered by a TDE jet, or a non-relativistic outflow.

Finally, TDEs have displayed bumps or plateaus in their light curves at UV wavelengths, with a time-scale of 100–200 d due to a relativistic orbital pericentre of a TDE with a massive 10^7–10^8 $M_\odot$ SMBH (Leloudas et al. 2016; Wevers et al. 2019), and at optical wavelengths over time-scales of 300–600 d due to potential multiple interactions between a dense debris stream and the accretion disc (Cannizzaro et al. 2020). Such a temporary influx of UV/optical photons would be echoed by reprocessed emission in the IR, which might explain the plateau/bump feature in the IR light curve of AT 2017gbl and the resulting increase in temperature of the blackbody fitted to the IR data at +375 d past discovery shown in Fig. 16.

4.3.4 Rate estimate of AT 2017gbl-like events in LIRGs

In conclusion, based on the constraints imposed by the energy budget, peak outburst luminosity, and the observed time-scales of the radio light curve and IR echo, we favour a TDE scenario for AT 2017gbl as opposed to a CLAGN. The discovery of AT 2017gbl resulted from the SUNBIRD programme (Kool et al. 2018), where we monitored a sample of ∼40 nearby LIRGs in the near-IR for SNe. If we assume all AT 2017gbl-like TDEs would have been detected in the near-IR for ∼1 yr, the total control time (e.g. two epochs six months apart for a given LIRG would result in 1.5 yr control time) covered as part of SUNBIRD is 72.7 yr. Assuming a Poisson process and adopting the confidence limits of Gehrels (1986), we obtain an estimate for the rate of AT 2017gbl-like TDEs in LIRGs of 10^n LIRG^{-1} yr^{-1} with $n = -1.9^{+0.5}_{-0.8}$, with 1σ errors. While this estimate has significant uncertainties and further work is required to constrain it, it agrees with the TDE rate estimate of 10^{-2} LIRG^{-1} yr^{-1} obtained by Tadhunter et al. (2017) based on their detection of one TDE candidate as a result of two epochs of spectroscopic observations of a sample of 15 LIRGs. We note that our rough estimate should also be considered as a lower limit for the actual TDE rate in LIRGs assuming that not all the TDEs show such luminous and long-lasting IR emission. This rate estimate supports the notion that LIRGs exhibit an elevated TDE rate compared to field galaxies.

4.4 Alternative scenarios

We consider also a scenario where the source of AT 2017gbl is a sufficiently energetic SN in the BLR, as was suggested for a nuclear IR-luminous transient in W0948+0318 (Assef et al. 2018b). This would explain the observed spectral features of AT 2017gbl, since they would originate from the ionized BLR in the same way as in the TDE/CLAGN scenario, but this scenario is constrained by the radio properties in the same way as the SN scenario discussed in Section 4.1. Luminous nuclear transients with strong IR excess have been discovered in Seyfert galaxies. Kankare et al. (2017) offered two alternative interpretations for such an event, PS1-10adi: either an extremely energetic SN or a tidal disruption of a star, powered by shock interaction between expanding material and large quantities of surrounding dense matter. Additionally, Moriya et al. (2017) proposed a scenario where superluminous transients in AGN, such as the TDE candidate PS16dtm (sharing similarities with PS1-10adi), are powered by interaction between accretion-disc winds and clouds in the BLR, leading to luminosities of $\sim 10^{44}$ erg s^{-1} on time-scales of ∼100 d. However, with a direct line of sight to the transient event fully obscured, it is difficult to ascertain the viability of these less common scenarios.

5 SUMMARY AND CONCLUSIONS

In 2017 July, we discovered that the Northern nucleus of IRAS 23436+5257 had significantly brightened in near-IR Keck images compared to the previous epoch from 2016 October. This transient event AT 2017gbl was also detected in the optical, albeit much fainter, and steadily declined in brightness in the near-IR and optical during the first ∼300 d. Additionally, AT 2017gbl was detected in the mid-IR, both by comparing follow-up *Spitzer* imaging with archival epochs, as well as through inspection of archival AllWISE and NEOWISE-R data from the *WISE* telescope. The mid-IR light curves not only revealed AT 2017gbl, but also a small but significant decline in flux of the nucleus prior to AT 2017gbl. We showed that the host-subtracted IR SED of AT 2017gbl is well represented by a single expanding and cooling blackbody component. From this IR echo, a lower limit to the energy budget could be inferred of 7.3×10^{50} erg. Fitting the smooth evolution of the IR blackbody temperature also allowed us to constrain the peak outburst epoch of the underlying transient to ∼140 d before discovery, with a peak luminosity of $0.1-1 \times 10^{45}$ erg s^{-1}. Inspection of optical and near-IR spectroscopy obtained at early epochs showed a ∼2000 km s^{-1} broad component to the strong hydrogen, He I and O I emission lines. This broad component disappeared or had visibly decreased at later epochs, so we attribute this component to the transient event. In addition to the IR echo, it is clear that at early times there is optical emission in addition to the IR blackbody. We show that after correcting for a *V*-band extinction of 2.5 mag, which is inferred from the line ratio of the broad (transient) components of strong Paschen lines, this is well fitted by a blackbody with a temperature of 6500 K peaking at optical wavelengths. At radio wavelengths, AT 2017gbl was still rising at the discovery epoch, reaching the peak at 15.5 GHz ∼13–15 d past the discovery, while at 4.4/4.9 GHz it took 150–200 d. Our VLBI imaging showed an evolving compact source coincident with the host galaxy nucleus (to within 0.04 arcsec) as observed in the near-IR with AO.

We compared the observed properties of AT 2017gbl with three different scenarios that have sufficiently large energy budgets: an energetic SN, a CLAGN due to a dramatic accretion rate change of the AGN, and a TDE. In all scenarios the IR blackbody is well explained by an IR echo, where dust absorbs UV/optical light from the transient and reradiates in the IR. In the following, we summarize the main observational properties of AT 2017gbl that lead us to conclude a TDE as the most likely scenario for this transient:

(i) Based on radiative transfer modelling of the host galaxy IR SED, we expect the Northern nucleus of IRAS 23436+5257 to host an obscured AGN, where the line of sight towards the central engine is fully obscured at optical, near-, and mid-IR wavelengths. The amplitude and time-scale of the pre-outburst mid-IR variability of the Northern nucleus can be explained by the presence of an AGN, but the outburst related to AT 2017gbl does not fit with 'normal' AGN variability.

(ii) The energy budget, the luminosity of the IR echo, and the spectral features of AT 2017gbl can be explained by a (super)luminous Type IIn SN such as SN 2010jl and SN 2015da. These supernovae also show prominent IR echoes, but require extreme mass-loss rates of the order of $\sim 0.1\,M_\odot$ yr^{-1} to explain their properties. However, based on the evolution and luminosity of the radio counterpart of AT 2017gbl, such a high mass-loss rate is ruled out. As such, we conclude that AT 2017gbl is unlikely to be a SN.

(iii) If AT 2017gbl is related to the central SMBH, either as a TDE of a star or a dramatic change in the accretion rate of an AGN (as seen in CLAGN), we should not be able to observe the event directly

in the optical, near- and mid-IR due to the strong obscuration by the dusty torus. In this case the observed optical emission is interpreted as scattered light from polar clouds, having originated from the transient itself and in the BLR. This is supported by the fitted optical blackbody temperature of 6500 K and the $\sim$2000 km s^{-1} broad emission lines, which are not compatible with those of optically discovered TDE candidates, but are consistent with being dominated by emission originated in the BLR. Similarly, the spectral signatures (Paschen $\alpha/\beta/\delta$, He I, O I) we have attributed to the transient event are observed in AGN BLR.

(iv) As TDEs and CLAGN are governed by similar physics, it is challenging to discern between the two scenarios. In the case of AT 2017gbl, the main ways to differentiate are the evolution time-scales in the optical, mid-IR, and radio. The rise to peak of the IR echo of AT 2017gbl is constrained to $\lesssim$140 d, and the following fast optical decline ($\sim$1 mag in 100 d) is traced by near-IR *J*-band, after subtraction of the IR echo contribution, to <370 d. In comparison with known CLAGN, these time-scales are extremely fast, while they match well with the optical time-scales of TDEs. In particular ASASSN-14li evolved in the optical and IR over time-scales similar to AT 2017gbl, while also showing a strikingly similar evolution and luminosity at radio wavelengths. As such we find a TDE as the most plausible scenario to explain the observed properties of AT 2017gbl.

AT 2017gbl is the third TDE candidate to be discovered in a LIRG, after Arp 299-B AT1 in Arp 299 and the TDE candidate in IRAS F01004-2237. Like the TDE candidate discovered by Tadhunter et al. (2017) in IRAS F01004-2237, the discovery of AT 2017gbl is the product of a monitoring programme of only a modest sample of LIRGs. Finding a TDE in such a sample supports the suggestion that the rate of TDEs in LIRGs is orders of magnitudes larger than that in field galaxies. Furthermore, the discovery of TDEs in actively starforming galaxies such as LIRGs is in contrast with the apparent preference of optical TDE discoveries for post-starburst E+A galaxies (Arcavi et al. 2014; French et al. 2016). It is therefore possible that the current optical TDE sample is affected by a strong observational bias against detecting dust-obscured transients in galactic nuclei. The high fraction of E+A galaxies that have undergone a recent galaxy merger has been offered as an explanation for their TDE overabundance (French et al. 2016). Interestingly, LIRGs are often interacting systems (Väisänen et al. 2012) and the morphology of IRAS 23436+5257 hosting two nuclei suggests a recent or an ongoing interaction and major merger between two galaxies. Furthermore, the LIRG host of Arp 299-B AT1 is also undergoing a major merger. This is noteworthy as the fraction of galaxies undergoing mergers below a redshift z<1 is very low (Conselice, Yang & Bluck 2009). This would suggest that galaxy mergers may be the leading cause of elevated TDE rates both in E+A galaxies as well as in LIRGs. Both systematic monitoring of galaxy mergers and LIRGs and detailed galaxy merger simulations are therefore required to constrain their TDE rate to test this scenario.

ACKNOWLEDGEMENTS

We thank the anonymous referee for insightful comments and suggestions. We would like to thank Petri Väisänen and Seppo Laine for useful discussions on LIRG properties and *WISE* data analysis, respectively. We thank David Williams for scheduling the final AMI-LA epoch and Chi-Ho Chan for comments on the submitted version of the manuscript. ECK acknowledges support from the Gravitational Radiation and Electromagnetic Astrophysical Transients (GREAT) research environment funded by *Vetenskapsrädet* under project no. 2016-06012, financial support from the visitor and mobility program of the Finnish Centre for Astronomy with ESO (FINCA), funded by the Academy of Finland grant no. 306531, and support from The Wenner-Gren Foundations under project no. UPD2019-0070. TMR acknowledges the financial support of the Jenny and Antti Wihuri foundation and the Vilho, Yrjö and Kalle Väisälä Foundation of the Finnish Academy of Science and Letters. MPT acknowledges financial support from the State Agency for Research of the Spanish MCIU through the 'Center of Excellence Severo Ochoa' award to the Instituto de Astrofísica de Andalucía (SEV-2017-0709) and through grant PGC2018-098915-B-C21 (MCI/AEI/FEDER). CRC acknowledges support by the Chinese Academy of Sciences (CAS), through grant CAS16013 of the CAS South America Center for Astronomy (CASSACA) and Programa de Astronomía CONICYT, Chile. PGJ and GC acknowledge support from European Research Council Consolidator Grant 647208. MG is supported by the Polish NCN MAESTRO grant 2014/14/A/ST9/00121. GEA is the recipient of an Australian Research Council Discovery Early Career Researcher Award (project DE180100346) and acknowledges partial support through the Australian Research Council's *Discovery Projects* funding scheme (project DP200102471). ST acknowledges financial support from the Russian Foundation for Basic Research project 17-52-80139 BRICS-a. RMcD is the recipient of an Australian Research Council Future Fellowship Award (project number FT150100333). WL is supported by the David and Ellen Lee Fellowship at Caltech.

The NOT Unbiased Transient Survey 2 (NUTS2) is funded in part by the Instrument Center for Danish Astronomy.

This work is based in part on observations made with the Nordic Optical Telescope, operated by the Nordic Optical Telescope Scientific Association at the Observatorio del Roque de los Muchachos, La Palma, Spain, of the Instituto de Astrofisica de Canarias.

Some of the data (PI: S. Ryder; program IDs Z229N2L, Z271N2L) presented herein were obtained at the W. M. Keck Observatory, which is operated as a scientific partnership among the California Institute of Technology, the University of California, and the National Aeronautics and Space Administration. The Observatory was made possible by the generous financial support of the W. M. Keck Foundation. The authors wish to recognize and acknowledge the very significant cultural role and reverence that the summit of Maunakea has always had within the indigenous Hawaiian community. We are most fortunate to have the opportunity to conduct observations from this mountain.

We thank the Mullard Radio Astronomy Observatory for carrying out the AMI-LA observations.

This work is based in part on observations (PIs: E. Kool, K. Maeda; program IDs GN-2017B-DD-2, GN-2018B-FT-109) obtained at the Gemini Observatory, which is operated by the Association of Universities for Research in Astronomy, Inc., under a cooperative agreement with the NSF on behalf of the Gemini partnership: the National Science Foundation (United States), National Research Council (Canada), CONICYT (Chile), Ministerio de Ciencia, Tecnología e Innovación Productiva (Argentina), Ministério da Ciência, Tecnologia e Inovação (Brazil), and Korea Astronomy and Space Science Institute (Republic of Korea).

The scientific results reported in this article are based in part on observations (PI: T. Heikkilä; program ID 18208589) made by the *Chandra X-ray Observatory*, and this research has made use of the CIAO software package provided by the Chandra X-ray Center (CXC). This article includes results based on observations made by the *Neil Gehrels Swift observatory*. The authors thank *Chandra* and *Swift* teams for the approval and rapid scheduling of our observations.

This work is based in part on observations made with the William Herschel Telescope (WHT). The WHT is operated on the island of La Palma by the Isaac Newton Group of Telescopes in the Spanish Observatorio del Roque de los Muchachos of the Instituto de Astrofísica de Canarias. The ISIS and ACAM data were obtained as part of (17A)N4/N6, (18A)N4, and (18B)N5.

This work is based in part on observations (PI: S. Mattila; program IDs 13226, 14054) made with the *Spitzer* Space Telescope, which is operated by the Jet Propulsion Laboratory, California Institute of Technology under a contract with NASA. This publication makes use of data products from the Wide-field Infrared Survey Explorer, which is a joint project of the University of California, Los Angeles, and the Jet Propulsion Laboratory/California Institute of Technology, funded by the National Aeronautics and Space Administration. This publication also makes use of data products from NEOWISE, which is a project of the Jet Propulsion Laboratory/California Institute of Technology, funded by the Planetary Science Division of the National Aeronautics and Space Administration.

This work is based in part on observations from programs RP028B and BP225 (PI: M. Pérez-Torres) obtained with the European VLBI Network (EVN) and the Very Long Baseline Array (VLBA), respectively. The European VLBI Network is a joint facility of independent European, African, Asian, and North American radio astronomy institutes. The National Radio Astronomy Observatory is a facility of the National Science Foundation operated under cooperative agreement by Associated Universities, Inc.

This publication makes use of data products from the Two Micron All Sky Survey, which is a joint project of the University of Massachusetts and the Infrared Processing and Analysis Center/California Institute of Technology, funded by the National Aeronautics and Space Administration and the National Science Foundation.

Funding for the SDSS and SDSS-II has been provided by the Alfred P. Sloan Foundation, the Participating Institutions, the National Science Foundation, the U.S. Department of Energy, the National Aeronautics and Space Administration, the Japanese Monbukagakusho, the Max Planck Society, and the Higher Education Funding Council for England. The SDSS Web Site is http://www.sdss.org/.

The SDSS is managed by the Astrophysical Research Consortium for the Participating Institutions. The Participating Institutions are the American Museum of Natural History, Astrophysical Institute Potsdam, University of Basel, University of Cambridge, Case Western Reserve University, University of Chicago, Drexel University, Fermilab, the Institute for Advanced Study, the Japan Participation Group, Johns Hopkins University, the Joint Institute for Nuclear Astrophysics, the Kavli Institute for Particle Astrophysics and Cosmology, the Korean Scientist Group, the Chinese Academy of Sciences (LAMOST), Los Alamos National Laboratory, the Max-Planck-Institute for Astronomy (MPIA), the Max-Planck-Institute for Astrophysics (MPA), New Mexico State University, Ohio State University, University of Pittsburgh, University of Portsmouth, Princeton University, the United States Naval Observatory, and the University of Washington.

DATA AVAILABILITY

The photometric data underlying this article are available in the article. The spectroscopic data will be made available on WISeREP[12] under the designation AT 2017gbl.

[12]https://wiserep.weizmann.ac.il/

REFERENCES

Abazajian K. N. et al., 2009, ApJS, 182, 543
Alard C., 2000, A&AS, 144, 363
Alard C., Lupton R. H., 1998, ApJ, 503, 325
Alexander K. D., Berger E., Guillochon J., Zauderer B. A., Williams P. K. G., 2016, ApJ, 819, L25
Alonso-Herrero A., Pereira-Santaella M., Rieke G. H., Rigopoulou D., 2012, ApJ, 744, 2
Andrews J. E. et al., 2011, AJ, 142, 45
Antonucci R. R. J., Miller J. S., 1985, ApJ, 297, 621
Arcavi I. et al., 2014, ApJ, 793, 38
Aretxaga I., Benetti S., Terlevich R. J., Fabian A. C., Cappellaro E., Turatto M., della Valle M., 1999, MNRAS, 309, 343
Armus L. et al., 2009, PASP, 121, 559
Asmus D., 2019, MNRAS, 489, 2177
Assef R. J., Stern D., Noirot G., Jun H. D., Cutri R. M., Eisenhardt P. R. M., 2018a, ApJS, 234, 23
Assef R. J. et al., 2018b, ApJ, 866, 26
Bade N., Komossa S., Dahlem M., 1996, A&A, 309, L35
Baldwin J. A., Phillips M. M., Terlevich R., 1981, PASP, 93, 5
Bertin E., 2006, in Gabriel C., Arviset C., Ponz D., Solano E., eds, ASP Conf. Ser. Vol. 351, Automatic Astrometric and Photometric Calibration with SCAMP. Astron. Soc. Pac., San Francisco, p. 112
Bowen I. S., 1947, PASP, 59, 196
Bright J., Fender R., Anderson G., Cantwell T., 2017, Astron. Telegram, 10679, 1
Bright J. S. et al., 2018, MNRAS, 475, 4011
Burston A. J., Ward M. J., Davies R. I., 2001, MNRAS, 326, 403
Cannizzaro G. et al., 2020, MNRAS, 493, 477
Cappellari M., 2017, MNRAS, 466, 798
Cappellari M., Emsellem E., 2004, PASP, 116, 138
Cardelli J. A., Clayton G. C., Mathis J. S., 1989, ApJ, 345, 245
Cen R., 2020, ApJ, 888, L14
Chambers K. C. et al., 2016, preprint (arXiv:1612.05560)
Chandra P., Chevalier R. A., Chugai N., Fransson C., Soderberg A. M., 2015, ApJ, 810, 32
Chan C.-H., Piran T., Krolik J. H., Saban D., 2019, ApJ, 881, 113
Chen X., Madau P., Sesana A., Liu F. K., 2009, ApJ, 697, L149
Chevalier R. A., 1998, ApJ, 499, 810
Chu J. K. et al., 2017, ApJS, 229, 25
Condon J. J., Cotton W. D., Greisen E. W., Yin Q. F., Perley R. A., Taylor G. B., Broderick J. J., 1998, AJ, 115, 1693
Conselice C. J., Yang C., Bluck A. F. L., 2009, MNRAS, 394, 1956
Cushing M. C., Vacca W. D., Rayner J. T., 2004, PASP, 116, 362
De Colle F., Lu W., 2020, New Astronomy Reviews, 89, 101538
Delhaize J. et al., 2017, A&A, 602, A4
Denney K. D. et al., 2014, ApJ, 796, 134
Djupvik A. A., Andersen J., 2010, Astrophys. Space Sci. Proc., 14, 211
Dou L., Wang T.-g., Jiang N., Yang C., Lyu J., Zhou H., 2016, ApJ, 832, 188
Dou L., Wang T., Yan L., Jiang N., Yang C., Cutri R. M., Mainzer A., Peng B., 2017, ApJ, 841, L8
Draine B. T., 2011, ApJ, 732, 100
Draine B. T., Lee H. M., 1984, ApJ, 285, 89
Dressler A., Gunn J. E., 1983, ApJ, 270, 7
Efstathiou A., Rowan-Robinson M., 1995, MNRAS, 273, 649
Efstathiou A., Siebenmorgen R., 2009, A&A, 502, 541
Efstathiou A., Rowan-Robinson M., Siebenmorgen R., 2000, MNRAS, 313, 734
Eracleous M., Livio M., Halpern J. P., Storchi-Bergmann T., 1995, ApJ, 438, 610
Erben T. et al., 2005, Astron. Nachr., 326, 432
Flewelling H. A. et al., 2016, preprint (arXiv:1612.05243)
Foreman-Mackey D., Hogg D. W., Lang D., Goodman J., 2013, PASP, 125, 306

Fox O. D. et al., 2011, ApJ, 741, 7
Fox O. D., Filippenko A. V., Skrutskie M. F., Silverman J. M., Ganeshalingam M., Cenko S. B., Clubb K. I., 2013, AJ, 146, 2
Fransson C. et al., 2014, ApJ, 797, 118
Frederick S. et al., 2019, ApJ, 883, 31
French K. D., Arcavi I., Zabludoff A., 2016, ApJ, 818, L21
French K. D., Arcavi I., Zabludoff A. I., Stone N., Hiramatsu D., van Velzen S., McCully C., Jiang N., 2020, ApJ, 891, 93
Gal-Yam A., 2019, ARA&A, 57, 305
Gaskell C. M., 2017, MNRAS, 467, 226
Gehrels N., 1986, ApJ, 303, 336
Gezari S. et al., 2012, Nature, 485, 217
Glass I. S., 2004, MNRAS, 350, 1049
Goodrich R. W., 1989, ApJ, 340, 190
Graham M. J. et al., 2020, MNRAS, 491, 4925
Gromadzki M. et al., 2019, A&A, 622, L2
Herrero-Illana R. et al., 2017, MNRAS, 471, 1634
HI4PI Collaboration, 2016, A&A, 594, A116
Hickish J. et al., 2018, MNRAS, 475, 5677
Hills J. G., 1975, Nature, 254, 295
Holoien T. W. S. et al., 2016, MNRAS, 455, 2918
Hung T. et al., 2017, ApJ, 842, 29
Inami H. et al., 2013, ApJ, 777, 156
Inserra C. et al., 2018, MNRAS, 475, 1046
Jarrett T. H. et al., 2011, ApJ, 735, 112
Jiang N., Dou L., Wang T., Yang C., Lyu J., Zhou H., 2016, ApJ, 828, L14
Jiang N. et al., 2017, ApJ, 850, 63
Jiang N., Wang T., Mou G., Liu H., Dou L., Sheng Z., Wang Y., 2019, ApJ, 871, 15
Johnson S. P., Wilson G. W., Tang Y., Scott K. S., 2013, MNRAS, 436, 2535
Kankare E. et al., 2012, ApJ, 744, L19
Kankare E. et al., 2017, Nat. Astron., 1, 865
Kelly B. C., Bechtold J., Siemiginowska A., 2009, ApJ, 698, 895
Kewley L. J., Groves B., Kauffmann G., Heckman T., 2006, MNRAS, 372, 961
Koay J. Y., Vestergaard M., Bignall H. E., Reynolds C., Peterson B. M., 2016, MNRAS, 460, 304
Kool E. C. et al., 2017, Astron. Telegram, 10651, 1
Kool E. C. et al., 2018, MNRAS, 473, 5641
Kormendy J., Ho L. C., 2013, ARA&A, 51, 511
Koshida S. et al., 2014, ApJ, 788, 159
Koss M., Mushotzky R., Baumgartner W., Veilleux S., Tueller J., Markwardt C., Casey C. M., 2013, ApJ, 765, L26
Kozłowski S., Kochanek C. S., Ashby M. L. N., Assef R. J., Brodwin M., Eisenhardt P. R., Jannuzi B. T., Stern D., 2016, ApJ, 817, 119
Lacy M. et al., 2020, PASP, 132, 035001
Lamperti I. et al., 2017, MNRAS, 467, 540
Landt H., Bentz M. C., Ward M. J., Elvis M., Peterson B. M., Korista K. T., Karovska M., 2008, ApJS, 174, 282
Larkin J. E., Armus L., Knop R. A., Soifer B. T., Matthews K., 1998, ApJS, 114, 59
Law-Smith J., MacLeod M., Guillochon J., Macias P., Ramirez-Ruiz E., 2017, ApJ, 841, 132
Lebouteiller V., Barry D. J., Spoon H. W. W., Bernard-Salas J., Sloan G. C., Houck J. R., Weedman D. W., 2011, ApJS, 196, 8
Leloudas G. et al., 2016, Nat. Astron., 1, 0002
Lopez-Rodriguez E. et al., 2018, ApJ, 859, 99
Lu W., Bonnerot C., 2020, MNRAS, 492, 686
Lu W., Kumar P., Evans N. J., 2016, MNRAS, 458, 575
MacLeod C. L. et al., 2016, MNRAS, 457, 389
MacLeod C. L. et al., 2019, ApJ, 874, 8
Mainzer A. et al., 2011, ApJ, 731, 53
Mainzer A. et al., 2014, ApJ, 792, 30
Marin F., 2018, MNRAS, 479, 3142
Mason R. E. et al., 2015, ApJS, 217, 13
Mattila S., Meikle W. P. S., 2001, MNRAS, 324, 325
Mattila S. et al., 2012, ApJ, 756, 111
Mattila S. et al., 2018, Science, 361, 482
McElroy R. E. et al., 2016, A&A, 593, L8
Merloni A. et al., 2015, MNRAS, 452, 69
Metzger B. D., Stone N. C., 2016, MNRAS, 461, 948
Mineo S., Gilfanov M., Sunyaev R., 2012, MNRAS, 419, 2095
Mitsuda K. et al., 1984, PASJ, 36, 741
Moriya T. J., Tanaka M., Morokuma T., Ohsuga K., 2017, ApJ, 843, L19
Nicholl M. et al., 2020, Nat. Astron., 4, 893
Osterbrock D. E., 1989, Astrophysics of Gaseous Nebulae and Active Galactic Nuclei. University Science Books, Mill Valley, CA
Pérez-Torres M. A., Alberdi A., Colina L., Torrelles J. M., Panagia N., Wilson A., Kankare E., Mattila S., 2009a, MNRAS, 399, 1641
Pérez-Torres M. A., Romero-Cañizales C., Alberdi A., Polatidis A., 2009b, A&A, 507, L17
Perez-Torres M. et al., 2015, in Bourke T. L.et al., eds, Proc. Sci., Advancing Astrophysics with the Square Kilometre Array (AASKA14). SISSA, Trieste, PoS(AASKA14)060
Perez-Torres M., Kool E., Ryder S., Mattila S., Fraser M., Kankare E., 2017, Astron. Telegram, 10712, 1
Perrott Y. C., Scaife A. M. M., Green D. A., Grainge K. J. B., Hurley-Walker N., Jin T. Z., Rumsey C., Titterington D. J., 2015, MNRAS, 453, 1396
Peterson B. M. et al., 2004, ApJ, 613, 682
Predehl P., Schmitt J. H. M. M., 1995, A&A, 500, 459
Rees M. J., 1988, Nature, 333, 523
Riffel R., Rodríguez-Ardila A., Pastoriza M. G., 2006, A&A, 457, 61
Riffel R., Rodríguez-Ardila A., Aleman I., Brotherton M. S., Pastoriza M. G., Bonatto C., Dors O. L., 2013, MNRAS, 430, 2002
Riffel R. et al., 2019, MNRAS, 486, 3228
Riffel R. A. et al., 2015, MNRAS, 446, 2823
Rodríguez-Ardila A., Pastoriza M. G., Viegas S., Sigut T. A. A., Pradhan A. K., 2004, A&A, 425, 457
Rodríguez-Ardila A., Riffel R., Pastoriza M. G., 2005, MNRAS, 364, 1041
Rothberg B., Fischer J., 2010, ApJ, 712, 318
Sanders D. B., Mazzarella J. M., Kim D.-C., Surace J. A., Soifer B. T., 2003, AJ, 126, 1607
Schirmer M., 2013, ApJS, 209, 21
Schirmer M., Carrasco E. R., Pessev P., Garrel V., Winge C., Neichel B., Vidal F., 2015, ApJS, 217, 33
Schlafly E. F., Finkbeiner D. P., 2011, ApJ, 737, 103
Sheng Z., Wang T., Jiang N., Yang C., Yan L., Dou L., Peng B., 2017, ApJ, 846, L7
Sheng Z. et al., 2020, ApJ, 889, 46
Skrutskie M. F. et al., 2006, AJ, 131, 1163
Stern D. et al., 2018, ApJ, 864, 27
Stickel M., Lemke D., Klaas U., Krause O., Egner S., 2004, A&A, 422, 39
Strauss M. A., Huchra J. P., Davis M., Yahil A., Fisher K. B., Tonry J., 1992, ApJS, 83, 29
Stritzinger M. et al., 2012, ApJ, 756, 173
Strubbe L. E., Quataert E., 2009, MNRAS, 400, 2070
Sun L. et al., 2020, ApJ, 898, 129
Tadhunter C., Spence R., Rose M., Mullaney J., Crowther P., 2017, Nat. Astron., 1, 0061
Tartaglia L. et al., 2020, A&A, 635, A39
Tody D., 1993, in Hanisch R. J., Brissenden R. J. V., Barnes J., eds, ASP Conf. Ser. Vol. 52, Astronomical Data Analysis Software and Systems II. Astron. Soc. Pac., San Francisco, p. 173
Trakhtenbrot B. et al., 2019, Nat. Astron., 3, 242
U V. et al., 2019, ApJ, 871, 166
Utrobin V. P., 2007, A&A, 461, 233
Vacca W. D., Cushing M. C., Rayner J. T., 2003, PASP, 115, 389
Väisänen P. et al., 2012, J. Phys.: Conf. Ser., 372, 012045
Väisänen P., Reunanen J., Kotilainen J., Mattila S., Johansson P. H., Ramphul R., Romero-Cañizales C., Kuncarayakti H., 2017, MNRAS, 471, 2059
Valdés J. R., Berta S., Bressan A., Franceschini A., Rigopoulou D., Rodighiero G., 2005, A&A, 434, 149
van Dokkum P. G., 2001, PASP, 113, 1420
van Velzen S., 2018, ApJ, 852, 72
van Velzen S. et al., 2016a, Science, 351, 62
van Velzen S., Mendez A. J., Krolik J. H., Gorjian V., 2016b, ApJ, 829, 19

van Velzen S. et al., 2020, preprint (arXiv:2001.01409)
Vanderplas J., Connolly A., Ivezić Ž., Gray A., 2012, in Das K., Chawla N., Srivastava A., eds, Conference on Intelligent Data Understanding (CIDU). IEEE, Boulder, CO, p. 47
Wang T., Yan L., Dou L., Jiang N., Sheng Z., Yang C., 2018, MNRAS, 477, 2943
Weiler K. W., Panagia N., Montes M. J., Sramek R. A., 2002, ARA&A, 40, 387
Wevers T. et al., 2019, MNRAS, 488, 4816
Williams C. L., Panagia N., Van Dyk S. D., Lacey C. K., Weiler K. W., Sramek R. A., 2002, ApJ, 581, 396
Winge C., Riffel R. A., Storchi-Bergmann T., 2009, ApJS, 185, 186
Wizinowich P. L. et al., 2006, PASP, 118, 297
Yamada R., Oyabu S., Kaneda H., Yamagishi M., Ishihara D., Kim J. H., Im M., 2013, PASJ, 65, 103
Yan L. et al., 2019, ApJ, 874, 44
Yang Q. et al., 2018, ApJ, 862, 109
Yang Q., Shen Y., Liu X., Wu X.-B., Jiang L., Shangguan J., Graham M. J., Yao S., 2019, ApJ, 885, 110
Yaron O., Gal-Yam A., 2012, PASP, 124, 668
Zauderer B. A. et al., 2011, Nature, 476, 425
Zhang T. et al., 2012, AJ, 144, 131
Zwart J. T. L. et al., 2008, MNRAS, 391, 1545

APPENDIX A: PHOTOMETRIC AND SPECTROSCOPIC OBSERVATIONS

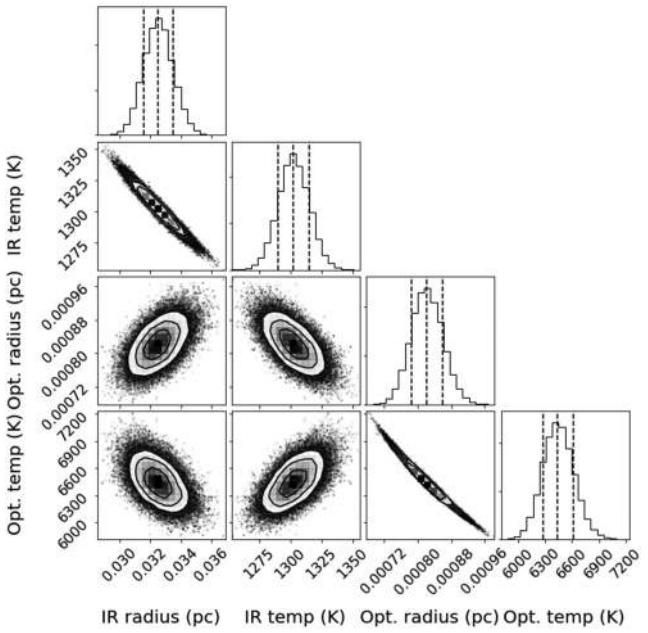

Figure A1. Corner plot of the posterior distributions of the MCMC two components fit to all optical, near-IR, and mid-IR fluxes of the epoch at +10 d, see Fig. 18. The fitted values are indicated by the center lines, with the 1σ confidence interval indicated on either side.

Table A1. AT 2017gbl near-IR photometry in apparent magnitudes in the Vega system. NIRC2 and NOTCam template epochs are indicated. A hyphen indicates the transient was observed, but not detected. An empty entry indicates the transient was not observed in the filter for that epoch.

UT Date	MJD	Epoch (d)	Telescope/Instrument	Magnitude		
				J	*H*	K_s
2016-10-21.4	57682.4	−260	Keck/NIRC2	template	template	template
2017-07-08.5	57942.5	discovery	Keck/NIRC2	16.03 ± 0.03	14.45 ± 0.04	13.22 ± 0.07
2017-07-27.2	57961.2	+19	NOT/NOTCam	16.18 ± 0.04	14.61 ± 0.03	13.27 ± 0.04
2017-08-19.2	57983.2	+41	NOT/NOTCam	16.50 ± 0.03	14.89 ± 0.03	13.48 ± 0.04
2017-09-03.9	57999.9	+57	NOT/NOTCam	16.81 ± 0.05	14.97 ± 0.03	13.58 ± 0.04
2017-09-29.9	58025.9	+83	NOT/NOTCam	16.90 ± 0.04	15.18 ± 0.05	13.68 ± 0.04
2017-10-17.1	58042.1	+100	NOT/NOTCam	17.19 ± 0.06	15.35 ± 0.04	13.87 ± 0.04
2017-12-05.2	58092.2	+150	Keck/NIRC2			14.26 ± 0.04
2018-01-03.9	58121.9	+179	NOT/NOTCam	18.14 ± 0.09	16.39 ± 0.08	14.68 ± 0.05
2018-01-22.8	58140.8	+198	NOT/NOTCam	18.08 ± 0.14	16.64 ± 0.07	14.84 ± 0.05
2018-05-12.2	58249.2	+307	NOT/NOTCam	19.23 ± 0.26	17.13 ± 0.12	15.61 ± 0.09
2018-07-14.1	58312.1	+370	NOT/NOTCam	-	17.10 ± 0.07	15.02 ± 0.03
2018-09-04.0	58364.0	+422	NOT/NOTCam	-	17.52 ± 0.10	15.59 ± 0.05
2018-09-24.1	58384.1	+442	NOT/NOTCam	-	17.98 ± 0.09	15.80 ± 0.04
2018-10-16.1	58406.1	+464	NOT/NOTCam	-	18.32 ± 0.17	16.12 ± 0.06
2018-11-03.9	58425.9	+483	NOT/NOTCam	-	18.59 ± 0.26	16.50 ± 0.09
2018-11-24.0	58445.0	+503	NOT/NOTCam	-	>19.2	16.48 ± 0.08
2018-12-10.9	58462.9	+520	NOT/NOTCam	-	-	16.43 ± 0.05
2018-12-30.9	58482.9	+540	NOT/NOTCam	-	-	16.57 ± 0.09
2019-01-10.9	58493.9	+551	NOT/NOTCam	-	-	16.61 ± 0.09
2019-02-18.9	58532.9	+590	NOT/NOTCam	-	-	16.85 ± 0.11
2019-07-04.2	58668.2	+726	NOT/NOTCam			>18.0
2019-07-22.9	58686.9	+744	NOT/NOTCam	template	template	
2019-09-14.1	58740.1	+798	NOT/NOTCam			template

Table A2. AT 2017gbl optical photometry in apparent magnitudes in the AB system. ACAM and ALFOSC template epochs are indicated. A hyphen indicates the transient was observed, but not detected. An empty entry indicates the transient was not observed in the filter for that epoch.

UT Date	MJD	Epoch (d)	Telescope/Instrument	Magnitude			
				g	*r*	*i*	*z*
2017-07-11.1	57945.1	+3	WHT/ACAM	21.22 ± 0.09	19.93 ± 0.02	19.08 ± 0.02	18.36 ± 0.03
2017-08-27.9	57992.9	+50	WHT/ACAM			19.66 ± 0.05	18.96 ± 0.05
2017-11-28.9	58085.9	+143	NOT/ALFOSC			20.79 ± 0.04	20.45 ± 0.03
2018-07-09.2	58308.2	+366	WHT/ACAM		-	-	-
2018-09-08.1	58369.1	+427	NOT/ALFOSC			template	template
2019-01-29.9	58512.9	+570	WHT/ACAM	template	template	template	template

Table A3. Mid-IR photometry of Northern nucleus of IRAS 23436+5257, observed with *Spitzer*.

UT Date	MJD	Epoch (d)	Telescope	Magnitude	
				3.6 μm	4.5 μm
2004-12-15.0	53354.0	−4589	*Spitzer*	11.14 ± 0.05	10.68 ± 0.05
2011-01-26.6	55587.6	−2355	*Spitzer*	11.24 ± 0.05	10.84 ± 0.06
2017-11-13.1	58070.1	+128	*Spitzer*	10.75 ± 0.05	10.19 ± 0.05
2017-12-19.8	58106.8	+164	*Spitzer*	10.82 ± 0.05	10.26 ± 0.05
2018-03-23.5	58200.5	+258	*Spitzer*	10.92 ± 0.05	10.36 ± 0.05
2018-05-17.1	58255.1	+313	*Spitzer*	10.93 ± 0.05	10.36 ± 0.06
2018-11-12.6	58434.6	+492	*Spitzer*	11.03 ± 0.05	10.46 ± 0.06
2019-04-01.5	58574.5	+632	*Spitzer*	11.11 ± 0.05	10.52 ± 0.06
2019-11-10.3	58797.3	+855	*Spitzer*	11.13 ± 0.05	10.61 ± 0.05

Table A4. Mid-IR photometry of IRAS 23436+5257, observed with *WISE*.

UT Date	MJD	Epoch (d)	Mission	Magnitude	
				3.4 μm	4.6 μm
2010-01-12.8	55208.8	− 2733	AllWISE	10.87 ± 0.03	10.20 ± 0.03
2010-07-18.4	55395.4	− 2547	AllWISE	10.89 ± 0.03	10.25 ± 0.03
2011-01-10.6	55571.6	− 2371	AllWISE	10.94 ± 0.03	10.32 ± 0.03
2014-01-14.4	56671.4	− 1271	NEOWISE-R	10.96 ± 0.03	10.35 ± 0.03
2014-07-22.0	56860.0	− 1083	NEOWISE-R	10.98 ± 0.03	10.40 ± 0.03
2015-01-12.8	57034.8	− 908	NEOWISE-R	11.00 ± 0.03	10.42 ± 0.03
2015-07-19.2	57222.2	− 720	NEOWISE-R	11.00 ± 0.03	10.44 ± 0.03
2016-01-07.9	57394.9	− 548	NEOWISE-R	11.04 ± 0.03	10.43 ± 0.03
2016-07-17.4	57586.4	− 356	NEOWISE-R	11.04 ± 0.03	10.43 ± 0.03
2017-01-01.5	57754.5	− 188	NEOWISE-R	11.07 ± 0.03	10.47 ± 0.03
2017-07-18.3	57952.3	+10	NEOWISE-R	10.56 ± 0.03	9.92 ± 0.03
2017-12-30.0	58117.0	+175	NEOWISE-R	10.76 ± 0.03	10.01 ± 0.03
2018-07-18.6	58317.6	+375	NEOWISE-R	10.83 ± 0.03	10.11 ± 0.03

Table A5. AT 2017gbl host-subtracted mid-IR photometry.

UT Date	MJD	Epoch (d)	Telescope	Magnitude	
				3.6 μm	4.5 μm
2017-11-13.1	58070.1	+128	*Spitzer*	11.8 ± 0.13	11.11 ± 0.12
2017-12-19.8	58106.8	+164	*Spitzer*	12.0 ± 0.15	11.28 ± 0.13
2018-03-23.5	58200.5	+258	*Spitzer*	12.32 ± 0.18	11.56 ± 0.15
2018-05-17.1	58255.1	+313	*Spitzer*	12.36 ± 0.19	11.56 ± 0.18
2018-11-12.6	58434.6	+492	*Spitzer*	12.79 ± 0.25	11.9 ± 0.23
2019-04-01.5	58574.5	+632	*Spitzer*	13.28 ± 0.37	12.14 ± 0.27
2019-11-10.3	58797.3	+855	*Spitzer*	13.43 ± 0.42	12.61 ± 0.32
				3.4 μm	4.6 μm
2017-07-18.3	57952.3	+10	*WISE*	11.64 ± 0.07	10.94 ± 0.08
2017-12-30.0	58117.0	+175	*WISE*	12.33 ± 0.12	11.2 ± 0.09
2018-07-18.6	58317.6	+375	*WISE*	12.65 ± 0.15	11.51 ± 0.11

Table A6. Log of spectroscopic observations of AT 2017gbl or its host IRAS 23436+5257. Resolving powers were taken from the instrument descriptions available online, and were compared against skylines in our data to check for consistency.

UT Date	MJD	Epoch (days)	Telescope	Instrument	Range (μm)	Resolving power
2016−11−18	57710	− 232	Keck	OSIRIS	1.96–2.30	–
2017−07−10	57944	+2	WHT	ISIS	0.35–0.80	900
2017−08−30	57995	+53	WHT	ISIS	0.35–0.80	1800
2017−09−01	57997	+55	Gemini N	GNIRS	0.85–2.50	1300–1400
2017−10−28	58054	+112	IRTF	SpeX	0.8–2.40	–
2018−11−23	58445	+503	Gemini N	GNIRS	0.85–2.50	1300–1400
2019−01−14	58497	+555	NOT	ALFOSC	0.32–0.96	360
2019−08−20	58715	+773	NOT	ALFOSC	0.57–0.86	1000

Table A7. Properties of the radio observations towards IRAS 23436+5257. Columns (1–3) list the observation date in UTC and MJD formats, and the days after discovery, (4) the radio array, (5) the central frequency, (6) the measured total flux density, (7) the flux density of AT 2017gbl after correcting the AMI and the VLA observations for the host contribution (see the text), and (8) the corresponding luminosity.

UT Date	MJD	Epoch (d)	Array	Frequency (GHz)	Total flux density (mJy)	AT 2017gbl Flux density (mJy)	AT 2017gbl Luminosity ($\times 10^{28}$ erg s^{-1} Hz^{-1})
(1)	(2)	(3)	(4)	(5)	(6)	(7)	(8)
1995-03-12	49788	− 8154	VLA	1.4	18.70 ± 1.85	–	–
2017-07-13	57947	+5	AMI	15.5	5.95 ± 0.30	2.35 ± 0.37	5.99 ± 0.94
2017-07-29	57963	+21	AMI	15.5	6.88 ± 0.35	3.28 ± 0.41	8.36 ± 1.05
2017-08-10	57975	+33	AMI	15.5	6.78 ± 0.34	3.18 ± 0.42	8.11 ± 1.08
2017-08-15	57980	+38	VLBA	4.4	0.93 ± 0.06	0.93 ± 0.06	2.37 ± 0.15
2017-08-15	57980	+38	VLBA	7.6	1.81 ± 0.10	1.81 ± 0.10	4.62 ± 0.26
2017-10-15	58041	+99	VLBA	4.4	2.03 ± 0.11	2.03 ± 0.11	5.18 ± 0.28
2017-10-15	58041	+99	VLBA	7.6	2.70 ± 0.14	2.70 ± 0.14	6.89 ± 0.36
2018-02-27	58176	+234	AMI	15.5	5.15 ± 0.26	1.55 ± 0.33	3.95 ± 0.83
2019-02-15	58529	+587	EVN	4.9	0.77 ± 0.08	0.77 ± 0.08	1.96 ± 0.20
2019-05-02	58605	+663	VLA	3.0	11.63 ± 1.95	<6.60	<16.83
2019-11-03	58790	+848	AMI	15.5	3.56 ± 0.18	–	–
2020-01-30	58878	+936	AMI	15.5	3.64 ± 0.19	–	–

[1]*The Oskar Klein Centre, Department of Astronomy, Stockholm University, AlbaNova, SE-10691 Stockholm, Sweden*
[2]*Department of Physics and Astronomy, Macquarie University, NSW 2109 Sydney, Australia*
[3]*Tuorla observatory, Department of Physics and Astronomy, University of Turku, FI-20014 Turku, Finland*
[4]*Instituto de Astrofísica de Andalucía (CSIC), Glorieta de la Astronomía s/n, E-18080 Granada, Spain*
[5]*School of Sciences, European University Cyprus, Diogenes Street, Engomi, 1516 Nicosia, Cyprus*
[6]*Núcleo de Astronomía de la Facultad de Ingeniería y Ciencias, Universidad Diego Portales, Av. Ejército 441, Santiago, Chile*
[7]*IAA, Academia Sinica, 11F of Astronomy-Mathematics Building, AS/NTU No. 1, Section 4, Roosevelt Rd, Taipei 10617, Taiwan, R.O.C*
[8]*TAPIR, Walter Burke Institute for Theoretical Physics, Mail Code 350-17, Caltech, Pasadena, CA 91125, USA*
[9]*International Centre for Radio Astronomy Research, Curtin University, GPO Box U1987, Perth, WA 6845, Australia*
[10]*Finnish Centre for Astronomy with ESO (FINCA), University of Turku, Vesilinnantie 5, FI-20014 Turku, Finland*
[11]*Aalto University Metsähovi Radio Observatory, Metsähovintie 114, FI-02540 Kylmälä, Finland*
[12]*Department of Physics, University of Oxford, OX1 3RH Oxford, UK*
[13]*Department of Astrophysics/IMAPP, Radboud University, P.O. Box 9010, NL-6500 GL Nijmegen, the Netherlands*
[14]*SRON, Netherlands Institute for Space Research, Sorbonnelaan 2, NL-3584 CA Utrecht, the Netherlands*
[15]*School of Physics, O'Brien Centre for Science North, University College Dublin, Belfield, Dublin 4, Ireland*
[16]*Astronomical Observatory, University of Warsaw, Al. Ujaz-dowskie 4, PL-00-478 Warszawa, Poland*
[17]*Department of Astronomy, Kyoto University, Kitashirakawa-Oiwake-cho, Sakyo-ku, Kyoto 606-8502, Japan*
[18]*Ritter Astrophysical Research Center, University of Toledo, Toledo, OH 43606, USA*
[19]*ARC Centre of Excellence for All Sky Astrophysics in 3 Dimensions (ASTRO 3D)*
[20]*INAF Osservatorio Astronomico di Padova, Vicolo dell'Osservatorio 5, I-35122 Padova, Italy*
[21]*Millennium Institute of Astrophysics (MAS), Nuncio Monseñor Sotero Sanz 100, Providencia, Santiago, Chile*
[22]*Departamento de Ciencias Fisicas, Universidad Andres Bello, Fernandez Concha 700, Las Condes, Santiago, Chile*
[23]*Department of Physics, Florida State University, 77 Chieftan Way, Tallahassee, FL 32306, USA*
[24]*Space Research Institute of the Russian Academy of Sciences, Profsoyuznaya Str. 84/32, Moscow 117997, Russia*
[25]*Department of Physics and Astronomy, 4129 Frederick Reines Hall, University of California, Irvine, CA 92697, USA*
[26]*Institute of Astronomy, University of Cambridge, Madingley Road, Cambridge CB3 0HA, UK*

This paper has been typeset from a TEX/LATEX file prepared by the author.